



WADD TECHNICAL REPORT 60-800

AN EXPERIMENTAL STUDY ON MULTI-WALL STRUCTURES FOR SPACE VEHICLES

D. G. Younger

S. Lampert

*Aeronutronic, A Division of
Ford Motor Company*

JANUARY 1961

Flight Dynamics Laboratory
Contract Nr. AF 33(616)-6641
Project Nr. 1368
Task Nr. 14007

**WRIGHT AIR DEVELOPMENT DIVISION
AIR RESEARCH AND DEVELOPMENT COMMAND
UNITED STATES AIR FORCE
WRIGHT-PATTERSON AIR FORCE BASE, OHIO**

300 - March 1961 - 24-919

FOREWORD

This report was prepared by the Aeromechanics Department, Aeronutronic Division of Ford Motor Company, Ford Road, Newport Beach, California, on Air Force Contract AF 33(616)-6641, under Task 14007 of Project 1368, "Construction Techniques and Application of New Materials." This work was administered under the direction of the Configuration Research Section, Structures Branch, Flight Dynamics Laboratory, Wright Air Development Division. Mr. James R. Johnson was the task engineer for the laboratory.

Dr. S. Lampert and Mr. D. G. Younger, Jr., of the Ford Motor Company were responsible for the experimental study organization and technical direction of the work performed. In addition to the fore-mentioned, the principal contributors to this phase of the investigation were Messrs. P. S. Allen, R. M. Foster, and H. M. Kaysen.

This report contains the results of the experimental studies performed between 1 June 1960 and 30 November 1960. An initial report covering the analytical studies performed between 1 June 1959 and 31 May 1960 was published as WADD TR 60-503.

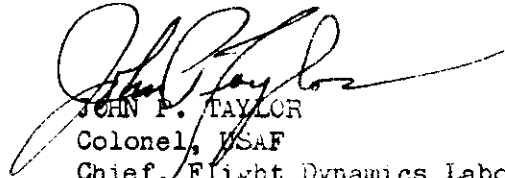
ABSTRACT

This report contains the results of an experimental study performed to evaluate the design techniques developed in an earlier report on this program, WADD TR 60-503. The structural index and design-constraint parameters reflecting the structural requirements for a manned space structure are evaluated, and a representative, cylindrical, double-wall shell is developed using the principles of minimum-weight design. Using specimens of half-scale cross-sectional dimensions, tests are performed on both wide columns and cylindrical shells.

PUBLICATION REVIEW

This report has been reviewed and is approved.

FOR THE COMMANDER:


JOHN P. TAYLOR
Colonel, USAF
Chief, Flight Dynamics Laboratory

WADD TR 60-800

iii

TABLE OF CONTENTS

<u>SECTION</u>		<u>PAGE</u>
1	INTRODUCTION	1
2	DETAIL DESIGN OF A REPRESENTATIVE DOUBLE-WALL SHELL	3
	2.1 Evaluation of a Representative Structural Index	3
	2.2 Evaluation of a Representative Skin Gage Constraint	6
	2.3 Evaluation of a Representative Core- Pitch Constraint	9
	2.4 Development of the Detailed Shell Geometry .	13
3	EXPERIMENTAL PROGRAM	18
	3.1 General Considerations	18
	3.2 Wide Column Test Program	19
	3.3 Cylindrical Shell Test Program	26
4	CONCLUSIONS	47
	REFERENCES	48
	APPENDICES:	
	A - GEOMETRICAL RELATIONSHIPS FOR CORRUGATED CORE DOUBLE-WALL CONSTRUCTION	49
	B - RELATIONSHIPS FOR METEOROID SHIELD DESIGN	52
	C - TEMPERATURE REGULATION IN A DOUBLE- WALL SPACE VEHICLE BY CONVECTIVE HEAT TRANSFER	54

LIST OF ILLUSTRATIONS

<u>FIGURE NO.</u>		<u>PAGE</u>
1	ESTIMATED PROBABILITIES OF METEOROID PENETRATIONS OF ALUMINUM	7
2	TEMPERATURE CHANGE IN A DOUBLE-WALL DUCT WITH FORCED CONVECTION INTERNALLY AND THERMAL IRRADIATION EXTERNALLY	10
3	MINIMUM-WEIGHT DESIGN CHART FOR CORRUGATED CORE SANDWICH PANELS HAVING SKIN-GAGE AND CORE-PITCH CONSTRAINT, $r_A = 0.4$	15
4	MINIMUM-WEIGHT DESIGN CHART FOR CORRUGATED CORE SANDWICH PANELS HAVING SKIN-GAGE AND CORE-AREA CONSTRAINT, $r_A = 0.4$	16
5	SECTION DETAILS OF CORRUGATED-CORE SANDWICH PANELS AND CYLINDERS	21
6	TYPICAL TEST SET-UP AND LOADING OF WIDE COLUMNS	23
7	COMPARISON OF THEORETICAL AND EXPERIMENTAL EFFICIENCIES OF TWO ALUMINUM ALLOY WIDE- COLUMN DESIGNS	24
8	STRESS-STRAIN RELATIONSHIPS FOR CORRUGATED CORE WIDE COLUMNS	27
9	TYPICAL TEST SET-UP FOR CYLINDRICAL SHELLS . . .	29
10	THE METHOD OF PRESSURIZING THE CYLINDRICAL SPECIMENS	31
11	STRESS-STRAIN RELATIONSHIP FOR UNPRESSURIZED CYLINDER #1 (Wall Section - 70° Core)	33
12	STRESS-STRAIN RELATIONSHIP FOR UNPRESSURIZED CYLINDER #4 (Wall Section - 45° Core)	34

LIST OF ILLUSTRATIONS (continued)

<u>FIGURE NO.</u>		<u>PAGE</u>
13	LOCAL BUCKLING DISPLAYED BY CYLINDER HAVING 45°-CORRUGATED CORE	35
14	STRESS-STRAIN RELATIONSHIPS FOR PRESSURIZED CYLINDER #2 (Wall Section - 70° Core)	36
15	STRESS-STRAIN RELATIONSHIPS FOR PRESSURIZED CYLINDER #3 (Wall Section - 70° Core)	37
16	STRESS-STRAIN RELATIONSHIPS FOR PRESSURIZED CYLINDER #5 (Wall Section - 45° Core)	38
17	MODE OF FAILURE TYPICAL OF CYLINDERS	40
18	ULTIMATE AND RESIDUAL STRENGTHS OF CYLINDERS . .	41
19	COMPARISON OF THE EFFICIENCY OF WIDE COLUMNS AND CYLINDERS HAVING IDENTICAL DOUBLE-WALL CROSS-SECTION	43
20	CRITICAL CRACK LENGTH FOR A PRESSURIZED UNSTIFFENED CYLINDER	46

SYMBOLS

METEOROID AND STRUCTURAL

A	cross-sectional area, in ²
b	plate width, in
c	column end-fixity coefficient
D	diameter, in
E	modulus of elasticity, lb/in ²
E _T	modulus of elasticity of target material, gram/cm ²
F	structural efficiency factor
I	moment of inertia, in ⁴
K _x	local buckling coefficient
L	true length, in
L _O	effective length, L/√c, in
M	bending moment, in-lb
m	mass of meteoroid particles, grams
N	number of meteoroid penetrations
\bar{N}	average number of meteoroid penetrations
P	total compressive load, lbs
p(N)	probability of N penetrations
q	compressive load intensity, lb/in
R	shell radius, in
r _A , r _b , r _t	structural proportions
t	thickness, in
v	velocity, ft/sec, km/sec
α, β	meteoroid environmental parameters
ε	mechanical strain, in/in
γ	meteoroid penetration parameter
μ	poisson's ratio
θ, φ	structural core element angles, degrees; also meteoroid penetration parameters
ρ	radius of gyration of double-wall cross-section, in
ρ _T	density of target material, gram/cm ³
ρ _p	density of meteoroid particle, gram/cm ³
σ	structural stress, lb/in ²
τ	design time interval, hrs.

Subscripts

A	attachment or joint
c	core element
cr	critical
i	per unit width of structure
pitch	per pitch length of corrugation
s	facing sheet (skin)
w	core sheet (web)

Contrails

THERMAL CONTROL

A	surface area or cross sectional area, in ² , ft ²
b _s	width of channel or facing sheet, in
c _p	specific heat, BTU/lb-°R
h	cross-section depth, in
h _c	convective film coefficient, BTU/hr-ft ² -°R
k	thermal conductivity, BTU/hr-ft-°R
N _{Pr}	Prandtl number ($c_p \mu / k$)
N _{ST}	Stanton number ($h_c / \rho V c_p$)
N _R	Reynolds number ($\rho V 4 r_h / \mu$)
P	pressure, psia
P _w	wetted perimeter, ft
q	rate of heat flow per unit area, BTU/hr-ft ²
R	thermal resistance, hr-ft ² -°R/BTU
r _h	hydraulic radius (A / P_w)
T	absolute temperature, °R
V	velocity, ft/sec
\dot{w}	mass flow rate, lb/sec
x	width of the exposed wetted surface of the duct, in
y _o	thickness of the double-wall facing sheet, in
Z	length L, of the duct or channel, in, ft
α	absorptivity of the double-wall surface
ϵ	emissivity of the double-wall surface
μ	absolute viscosity, lb/ft-sec
ρ	mass density, lb/ft ³
σ	Stefan-Boltzman constant (0.1714×10^{-8}), BTU/ft ² -hr-°R ⁴

Subscripts

b	bulk
e	earth irradiation
i	in
o	out
s	solar irradiation

SECTION 1

INTRODUCTION

In this program a guide-line study was performed which was aimed at highlighting the salient features influencing the design of rigid-type, double-wall structure for manned spacecraft. The studies included trajectories and loads, solar heating, behavior of materials, meteoroid and high energy radiation shielding, and the principles of minimum-weight structural design. The discussion of the results of the several study areas has been presented in WADD TR 60-503.

With regard to the application of the principles of minimum-weight structural design to double-wall structures, the above report emphasized that the stability calculations for complex structural geometries are complicated by serious analytical difficulties. Furthermore, it was pointed out that these difficulties lead to severe complications in the development of optimum design procedures. Therefore, it became expedient in the study to employ certain simplifying approximations, which by more rigorous theoretical considerations and on the basis of existing empirical information, were shown to be conservative.

In particular, the phenomena associated with the buckling of cylindrical shell structures are known to be complex and can be adequately described only in terms of the non-linear equations of finite deformation theory. To carry out fundamental analyses of these

Manuscript released by authors on 30 September 1960 for publication as a WADD Technical Report.

basic processes would involve excessively lengthy and extensive calculations in order to generate a quantity of data and information sufficient to be useful for design purposes. Such calculations were considered prohibitively time consuming, and therefore, in order to undertake immediate detailed studies of specific configurations, a more pragmatic and expedient approach was adopted. In line with the requirements of a "guide-line study", analyses and design methods and techniques were developed within the existing "state-of-the-art". An effort was made in the preceding report (WADD TR 60-503) to either adapt wide-column analyses to the study of moderately curved geometries, or to employ the classical, linear, "small deflection" theory in conjunction with an appropriately selected, conservative "reduction factor" to allow for the unfavorable effects of "snap-through" buckling. This avoided the severe mathematical difficulties inherent to the non-linear equations associated with the finite deformation theory and permitted the use of the simpler and more tractable, analytical expressions resulting from the wide-column or linear shell theory. This simplicity was achieved, of course, only at the expense of some compromise of structural efficiency and some restrictions on optimization.

In order to substantiate both the developed design techniques for the double-wall wide columns and to demonstrate the integrity of the more representative cylindrical double-wall shell structure, a rather modest experimental program was undertaken. The details and results of this experimental program are contained within this report. In carrying out the limited test program, specimens which were considered reasonably representative of the structural requirements of a typical manned spacecraft were employed. In the interests of completeness in this report, the discussion of test specimens and results is preceded by a presentation of the minimum-weight design procedures used in converging on the detail geometry of double-wall cross-section configurations.

SECTION 2

DETAIL DESIGN OF A
REPRESENTATIVE DOUBLE-WALL SHELL

2.1 EVALUATION OF A REPRESENTATIVE STRUCTURAL INDEX

The average failing stress of a longitudinally loaded structure can be expressed as a function of the load applied to the structure and the distance over which the load must be transmitted. Several parameters that relate load and distance have been suggested for longitudinally stiffened wide-columns, but the parameter that has been most widely used is $q/(L/\sqrt{c})$. This quantity is called the structural index. It is a measure of the loading intensity and has the dimensions of a stress indicative of a compressive load per inch, q , transferred over a distance, L . Once an optimum wide-column structure of a certain size has been designed or tested for a given load, its proportions may be used for any other combination of load and size which results in the same value of the structural index.

The problem of designing an optimum double-wall shell to support an axial compressive load requires a knowledge of the load, the distance over which the load must be transmitted, and the width over which the material must be distributed. Therefore, to develop the detail design of a double-wall configuration representative of that which meets the structural requirements of a typical manned space mission, a reasonable estimate must be made of the above mentioned design inputs, q and L/\sqrt{c} . In the following paragraphs the estimates leading to a structural index are made.

Contrails

For a cylindrical shell of diameter, D , and a uniform cross section, the beam-column theory gives the following equation for the maximum value of q when both an axial compressive load, P , and a bending moment, M , are acting on the section.

$$q = \frac{4M}{\pi D^2} + \frac{P}{\pi D} \quad (1)$$

A realistic value for the total axial load, P , commensurate with a typical 25,000 lb vehicle capable of being placed in a 300-mile circular earth orbit by a booster of the Saturn class has been given in Figure 6-4 of Reference 1. From the resultant curve shown in that figure the maximum value for P is found to be a compressive load of 100,000 lbs. This represents the axial load transmitted through the shell wall after the "lift off" tensile load due to an internal pressure of 7.5 lb/in² has been subtracted from the effective longitudinal inertia load.

The diameter, D , of the representative vehicle which allows a 6-foot tall man to stand upright on a walkway within the vehicle is selected as 80 inches.

The bending moment, M , in Equation (1) arises from the lateral forces that must be considered in the design of the structural shell. These forces may be the result of aerodynamic loads (wind shears and/or gusts) during ascent or the result of booster or control malfunction. For purposes of this design an applied bending moment induced by a 2 g lateral acceleration of the 25,000 lb vehicle was considered representative. The magnitude of the bending moment was taken as $5.85(10^6)$ in-lb. This value can be considered to be that which occurs in the shell wall just forward of the booster-payload interface located at a distance 117 inches aft of the c.g. The simultaneous occurrence of the peak bending moment and the maximum thrust load defines the limit load to be considered.

The limit load intensity, q_L , becomes

$$q_L = \frac{1}{\pi(80)} \left[\frac{4(5.85)(10^6)}{80} + 100,000 \right] = 1560 \text{ lb/in} \quad (2)$$

Contrails

If the usual definition of loads is employed, the limit loading, q_L , is the maximum expected to be encountered, and a factor of safety must be applied to establish the design load. A factor of safety of 1.25 has been considered applicable, and the design loading intensity is found to be

$$q_D = 1.25 q_L = 1950 \text{ lb/in} \quad (3)$$

To complete the definition of a representative structural index, $q/(L/\sqrt{c})$, requires the specification of a realistic effective length, L/\sqrt{c} , over which the loading can be considered to be transmitted. In the usual type of construction, the double wall shell is supported at intervals by frames or bulkheads. The spacing of such frames establishes the length of the several tandem compartments and the frame size can be expected to be dictated by other than minimum-weight shell wall considerations. For purposes of this design, the frame spacing of the aft compartment has been arbitrarily set at 69 inches. In addition, a column end restraint coefficient, c , equal to 2.0 has been selected as a realistic design value for double wall construction supported by sturdy frames.

With the above design requirements established, the evaluation of a typical structural index compatible with the loads and size of a representative manned space vehicle is computed to be

$$\frac{q_D}{L/\sqrt{c}} = \frac{1950}{69/\sqrt{2}} = 40 \text{ lb/in}^2 \quad (4)$$

In the design of structures satisfying several design requirements, the above value for the structural index must be supplemented with the definition of certain design constraint parameters. The incorporation of such additional design requirements in a minimum-weight study is most important. For example, requirements as to torsional stiffness, pressurization, or meteoroid resistance often dictate a minimum skin gage that must be incorporated as a "constraint" in the design of space structures.

In Reference 1 three constraint parameters were presented and their effects on minimum-weight structures were discussed. The design constraints considered were the skin-gage (facing sheet) parameter,

$$t_s \left(\frac{E}{qL_o} \right)^{\frac{1}{2}}$$

the core-pitch parameter,

$$b_s \left(\frac{E}{qL_o^3} \right)^{\frac{1}{4}}$$

and the core-area parameter,

$$A_c \left(\frac{E}{qL_o^3} \right)^{\frac{1}{2}}$$

where $L_o = L/\sqrt{c}$.

In Sections 2.2 and 2.3 discussions leading to the specification of a skin-gage and a core-pitch parameter are presented with emphasis on the magnitude of these constraints for the representative design.

2.2 EVALUATION OF A REPRESENTATIVE SKIN GAGE CONSTRAINT

Based on an analysis of the state-of-the-art information, the shielding requirements for meteoroid resistance have been assessed and presented in Reference 1. These studies were accomplished in light of the uncertainties in knowledge of the environment and the response of materials and structures to hypervelocity impact.

In the referenced report, design methods were developed for various design criteria and mission parameters. The effects of uncertainties in environmental and response parameters were investigated by varying these parameters over reasonable ranges. The results of these studies shed considerable light on some important aspects of the meteoroid problem.

Using reasonably conservative estimates, it appears that in order to achieve high probabilities of no meteoroid penetrations of relatively large surfaces exposed in space for even rather modest periods of time, a considerable thickness of "armor" is required. This fact is depicted graphically in Figure 1. In this figure the probability of a specified number of meteoroid penetrations is given as a function of an "exposure parameter" for several thicknesses of aluminum. The shielding

Reference Appendix B

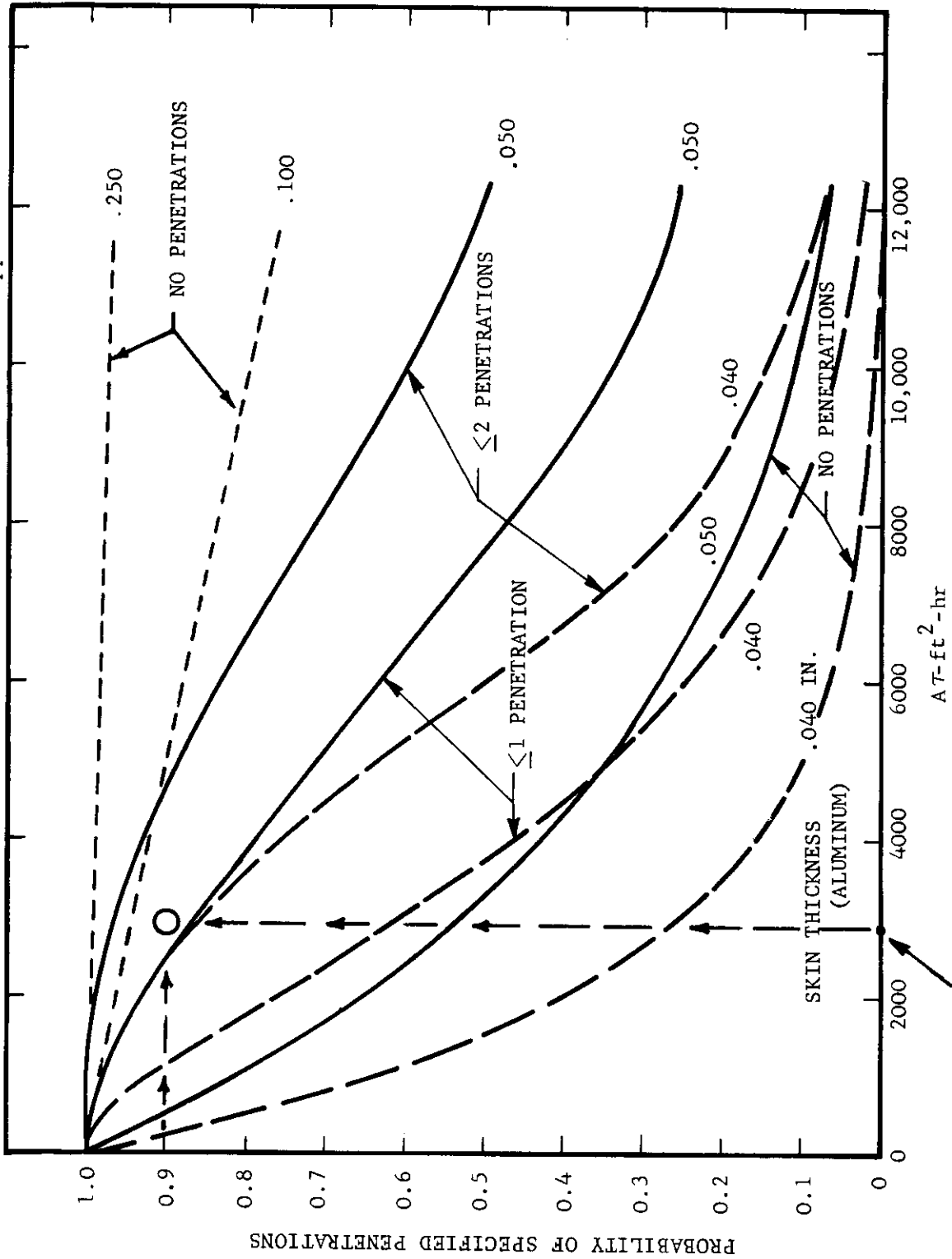


FIGURE 1. ESTIMATED PROBABILITIES OF METEOROID PENETRATIONS OF ALUMINUM

S2132

studies performed in Reference 1 have indicated that aluminum is among the metals which appear most resistant to penetration by meteoroids. As shown in Figure 1, skin gages greater than 0.10 inch are required in order to maintain high-reliability, puncture-free designs for reasonable exposure times.

It must be emphasized that the curves in Figure 1 are based upon conservative estimates which are reasonable in terms of current knowledge of the meteoroid environment of space and the present state of the art in hypervelocity penetration mechanics. The methods employed in meteoroid shielding design are developed in Reference 1 and the pertinent analyses and background information are presented there. However, the theoretical details which were used in the development of Figure 1 are included in Appendix B of this report.

As mentioned earlier, the aluminum alloys rank very high among the metals which are most efficient, on a weight basis, for shielding against penetration by meteoroids. Only beryllium and magnesium appear to be more efficient.

Figure 1 can be employed to estimate the skin thickness necessary to insure a specified level of resistance to meteoroid penetration of the vehicle's outer surface. The aft compartment of the vehicle under consideration has an exposed double-wall surface area of

$$A = \pi DL = \pi(80/12)(69/12) = 120 \text{ ft}^2 \quad (5)$$

The specification of τ , the design time interval, must be preceded by detailed reliability studies in which an applicable repair system is given careful consideration. The design time interval will seldom be defined as the total elapsed time of the mission. In general the time interval will be considerably less than the mission time and will be governed by the mechanics of the repair scheme and its ability to make reliable repairs at a given frequency. The necessary details concerning the many suggested methods of repair are as yet unavailable to the designer; therefore, as an expedient to the development of the present design, a time interval of 24 hours has been assigned to τ . The mission parameter, $A\tau$, then becomes

$$A\tau = 120 \times 24 = 2880 \text{ ft}^2\text{-hr} \quad (6)$$

For design purposes it is further specified that the compartment shell must insure a probability of 90 percent that no more than 2 penetrations will occur in the outer skin in any 24-hour period. Such a specification would indicate that a proven repair system can be made available which is capable of making 2 repairs per 24 hours with high reliability.

The above information is now sufficient to enter Figure 1 and determine a required skin gage for the vehicle compartment. The design point is shown on the figure where a skin gage of approximately 0.043 is indicated. Using the previously determined values for q and L/\sqrt{c} with the modulus of elasticity of aluminum, $E = 10.5(10^6)$ psi, and the $t_s = 0.043$ determined above, the skin-gage constraint parameter can be computed as follows:

$$t_s \left(\frac{E}{qL/\sqrt{c}} \right)^{\frac{1}{2}} = 0.043 \left[\frac{10.5(10^6)}{1950(69/\sqrt{2})} \right]^{\frac{1}{2}} = 0.45 \quad (7)$$

2.3 EVALUATION OF A REPRESENTATIVE CORE-PITCH CONSTRAINT

The problem of simulating a "shirt sleeve" environment in a manned space vehicle is one that must be solved with a minimum of complexity and a maximum of reliability. Passive thermal control systems, which by their very nature are highly reliable, cannot be expected to provide all the thermal control required in a manned space vehicle. Therefore, the passive system must be supplemented to some extent by an active thermal control system.

The double-wall structure provides a convenient means for active thermal control. It presents a simple heat exchanger surface that can be used for forced convection heating or cooling. The prime question to be answered in considering such an application is, what is the magnitude of convective heating required to maintain the internal wall temperature consistent with the shirt sleeve environment?

Assuming that there is negligible internal power generation, the function describing the temperature rise or drop in a double-wall of a given mass flow rate, and surface coating is plotted in Figure 2. The derivation and the assumptions associated with the development of Figure 2 are shown in Appendix C. In order to bracket the maximum convective heating and cooling requirements, the thermal irradiation in one case was

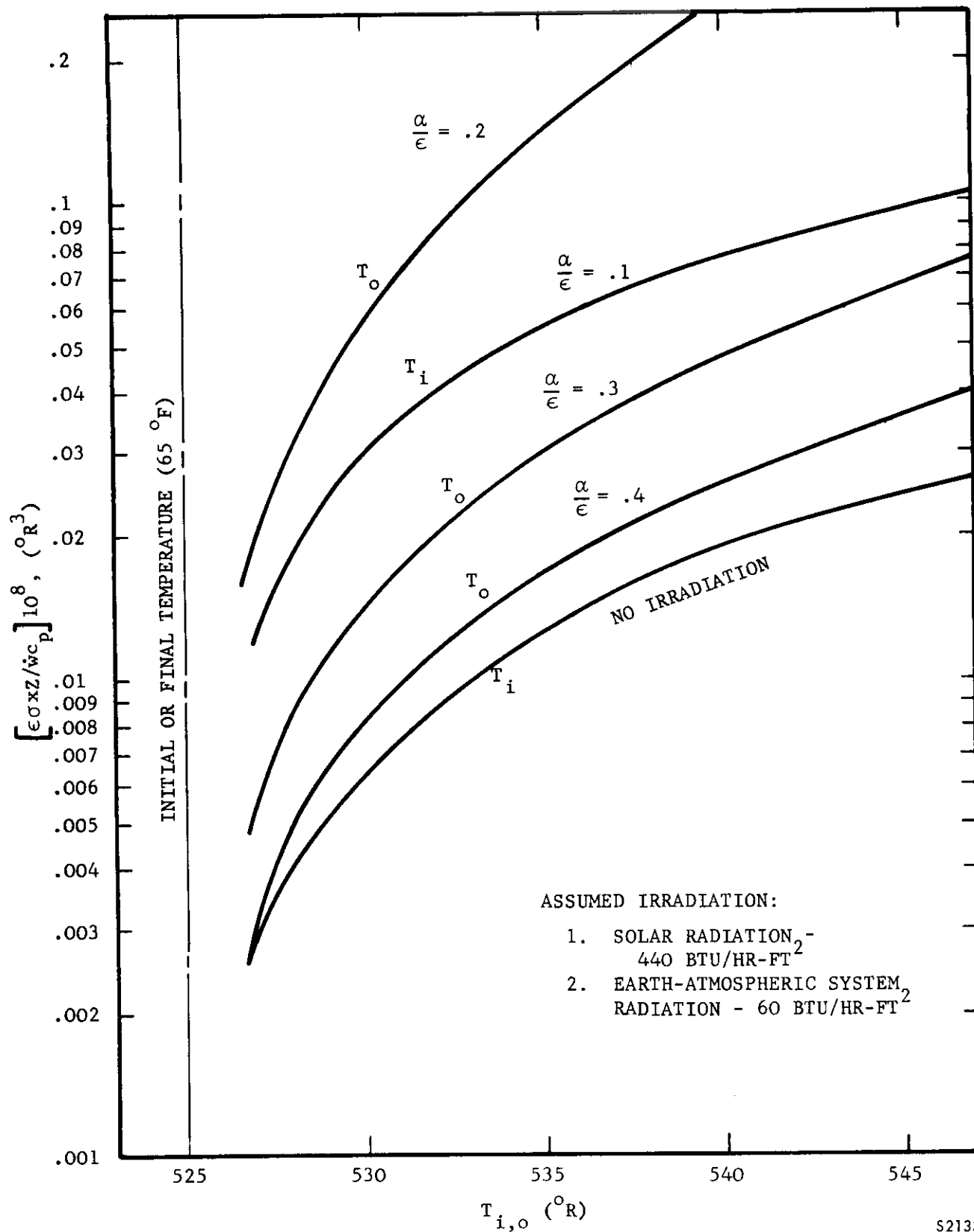


FIGURE 2. TEMPERATURE CHANGE IN A DOUBLE-WALL DUCT WITH FORCED CONVECTION INTERNALLY AND THERMAL IRRADIATION EXTERNALLY

assumed to be more severe than an earth satellite would normally encounter and in the other case, the thermal irradiation was assumed to be zero. It was also assumed that the space vehicle was to be maintained at a nominal internal temperature of 65°F (525°R). This temperature was chosen because, as indicated in Reference 2, 65°F is approximately the wall temperature required to simulate a shirt sleeve environment in a space vehicle.

Examination of Figure 2 indicates several features of double-wall convective heat transfer in outer space. For a given allowable temperature rise or drop, the mass flow rate required to regulate the vehicle temperature is proportional to the surface emissivity, the channel length, and the exposed channel width. For an α/ϵ surface coating equal to or greater than 0.2, the convective fluid cools the structure, but if $\alpha/\epsilon \leq 0.1$, the convective fluid must heat the structure. The maximum mass flow rate required for a given temperature regulation is established by the minimum value of the parameter, $(\epsilon \sigma x Z) / (\dot{w} c_p)$, experienced by the space vehicle during orbit. Since the vehicle surface coating can easily be made to have $\alpha/\epsilon < 0.4$, the critical mass flow rate may be required on the side of the vehicle that experiences no irradiation.

To develop a double-wall configuration representative of that which meets the thermal requirements of a typical manned space mission, it is necessary to make some realistic estimates of the required temperature regulation, the vehicle surface coating, the properties of the convective gas, the required mass flow rate, and the required duct geometry.

The nominal temperature required in the manned portion of the space vehicle is assumed to be 65°F , and the allowable temperature fluctuation has been limited to 2°F thus minimizing the temperature gradients affecting the shirt sleeve environment.

In order to minimize the convective cooling requirement when the vehicle is exposed to direct sunlight, the vehicle should be coated with a good solar reflector, preferably one that has performed reliably in outer space. Such a coating is Rokide A (aluminum oxide). It has the required thermal radiation properties ($\alpha/\epsilon = 0.195$, $\epsilon = 0.77$), and has proven to be reliable with the Explorer satellites.

It will be assumed that the double-wall convective heat transfer gas will be temperature conditioned in an internal air conditioning system. To avoid problems associated with toxic gases and system leaks, it will be assumed the double-wall convective heat transfer gas will be air at 65°F and 7.5 psia. Therefore the specific heat, $c_p = 0.24 \text{ BTU/lb-}^{\circ}\text{F}$.

In the particular system proposed, it is assumed that the capacity of the internal air condition system is such that there is a limit on the maximum mass flow in any double-wall duct. The actual limits would involve a system study and certain tradeoffs would be made between pump size, air conditioning capacity, pressure drop in the system and heat transfer effectiveness. For this particular design it is assumed that an optimum thermal system is obtained when the mass flow rate in any duct is equal to or less than 0.036 lb/sec.

With the above design requirements established, the evaluation of a typical core-pitch constraint compatible with the thermal requirements of a representative manned space vehicle can be made. The critical radiating wetted surface area associated with a given mass flow rate is determined by the channel width, b_s . Based on the maximum mass flow rate requirement, the critical value of the channel width is obtained when the parameter, $(\epsilon \sigma x Z) / (\dot{w}_p c_p)$, is a minimum. For the particular surface coating proposed here, the above parameter is a minimum when the space vehicle is in a position where no irradiation is impinging on the surface. From Figure 2 for no irradiation and $\Delta T = 2^\circ \text{F}$,

$$\frac{\epsilon \sigma x Z}{\dot{w}_p c_p} = 0.003(10^{-8}) \text{ } ^\circ \text{R}^{-3} \quad (8)$$

and the critical channel width

$$\begin{aligned} b_s &= x = 0.003(10^{-8}) \frac{\dot{w}_p c_p}{\epsilon \sigma Z} \\ &= \frac{0.003(10^{-8})(0.036)(0.24)}{0.77(0.476)(10^{-12})(5.75)} \\ &= 0.123 \text{ ft (or 1.48 in)} \end{aligned} \quad (9)$$

Therefore, a representative core-pitch constraint as defined in Section 2.1 is

$$b_s \left(\frac{E}{q L_o^3} \right)^{\frac{1}{4}} = 1.48 \left[\frac{10.5(10^6)}{1950(48.8)^3} \right]^{\frac{1}{4}} = 0.68 \quad (10)$$

2.4 DEVELOPMENT OF THE DETAILED SHELL GEOMETRY

The preceding discussions have led to the specification of three design parameters typical of the design requirements that may be imposed on a manned space structure. These parameters are (1) the structural index which accounts for the expected mechanical loads, (2) the skin-gage parameter which insures a specified level of resistance to meteoroid penetration, and (3) the core-pitch parameter which specifies the spacing of the longitudinal stiffening elements for heat exchanger applications.

In developing the detail design of the representative cylindrical shell, it has been convenient to arrange the design inputs into the following form,

$$q/L_o = 40 \text{ lbs/in}^2 \quad (\text{structural index})$$

$$t_s \left(\frac{E}{qL_o} \right)^{\frac{1}{2}} = 0.45 \quad (\text{skin-gage parameter})$$

$$b_s \left(\frac{E}{qL_o} \right)^{\frac{1}{4}} = 0.68 \quad (\text{core-pitch parameter})$$

As is the case in minimum-weight studies of this type the structural index is expressed in units of lb/in^2 and the constraint parameters are expressed non-dimensionally.

The magnitudes shown for the constraint parameters reflect the use of the 2024-T3 aluminum alloy in the shell design. The selection of the aluminum alloy was based upon a three-fold consideration; namely, the alloy is efficient for (1) the low loading intensity (structural index) specified here, (2) the exposure time and temperature range expected, and (3) the shielding applications against meteoroid penetration.

The selection of the superior basic type of cross-section for the double-wall shell should entail a careful study of the effect of design constraints on the structural efficiencies of a large number of possible configurations. These studies would, of course, require that a complete set of comprehensive charts be available to facilitate the choice of the most efficient configuration. A beginning in this direction was made in Reference 1. However, the design charts presented there are

Contrails

sufficiently extensive for only two configurations. These are the charts for the single-truss (Figure 6-9) and the double-truss (Figure 6-10) which enable weight penalties to be assessed after the introduction of two design constraints.

In the present report one additional configuration has been treated in sufficient detail to permit its inclusion in the evaluation study. This additional cross-section type is the corrugated core sandwich. Charts for this construction are presented in Figures 3 and 4. The geometrical relationships employed in the development of the contour-plots are given in Appendix A.

The most efficient of the three shell-wall configurations is determined by entering Figures 6-9 and 6-10 of Reference 1, and Figure 3 of this report with the specified values of the skin-gage and core-pitch parameters. At the intersection of the two parameters on each of the three figures, the structural efficiency, F , is determined. This procedure leads to efficiencies of 0.73, 0.72, and 0.76 for the single-truss, the double-truss, and the corrugated core, respectively. On the basis of these efficiencies the latter structural type is selected. Had the design-constraint parameters been sufficiently different from those employed here, it is very likely that one of the other configurations would have proven superior. In any case, for a given material and structural index, a percentage improvement in efficiency, F , constitutes an equal percentage reduction in weight.

If there were no design constraints injected into the comparison of the three basic configurations, the double-truss would have offered the superior efficiency, namely, 0.84 as compared to 0.77 and 0.83 displayed, respectively, by the single-truss and corrugated core. However, it must be emphasized that in the event that such unconstrained designs are found permissible, the designer can accept the peak efficiency only if he is also willing to accept the detailed geometry resulting from the corresponding design point on the charts.

The detailed design of the corrugated-core double-wall shell begins with the design point (center of dashed circle) on Figure 3. At the design point the following information is found,

$$\begin{aligned} F &= 0.76 \\ r_t &= 0.5 \\ r_b &= 0.93 \\ r_A &= 0.40 \end{aligned}$$

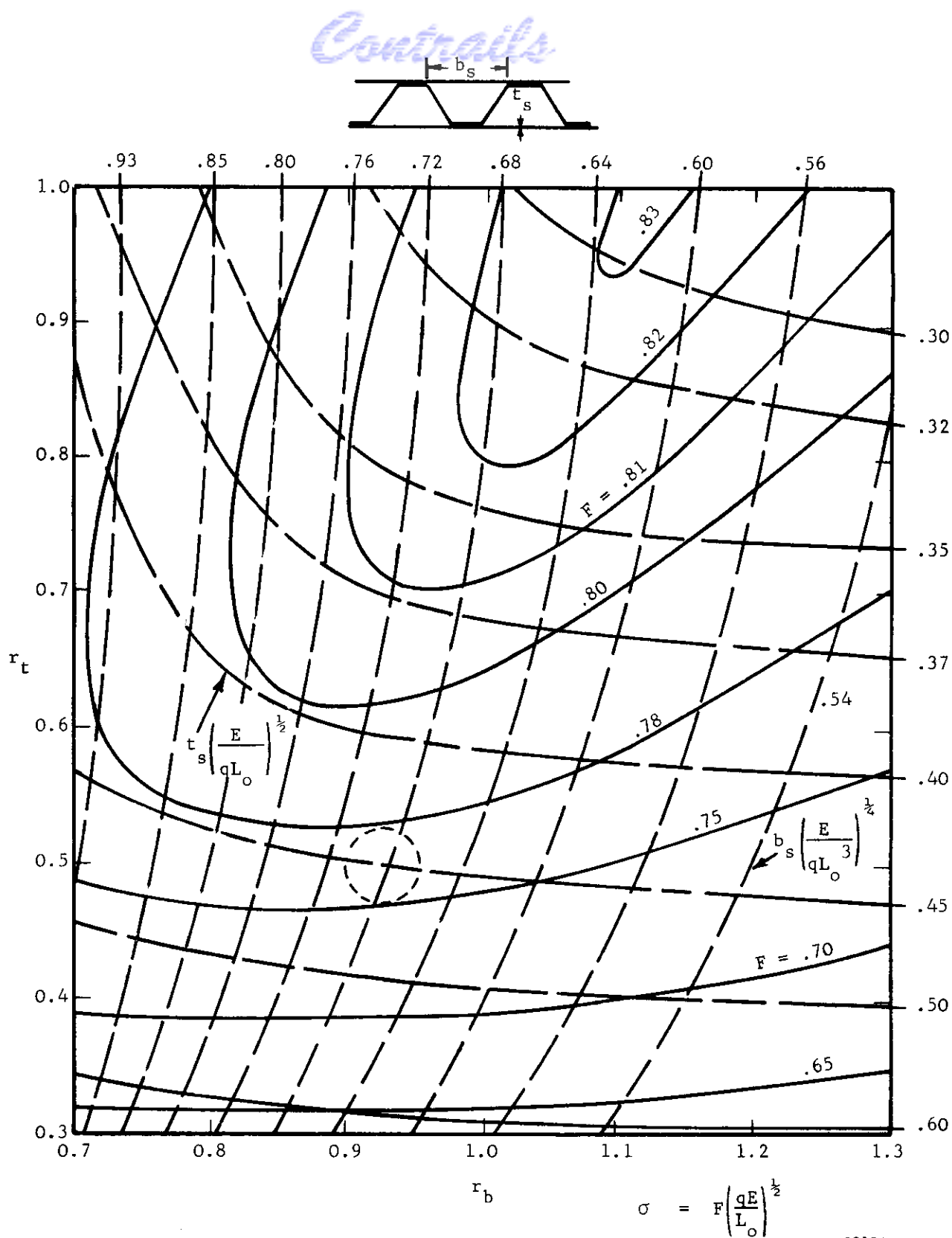
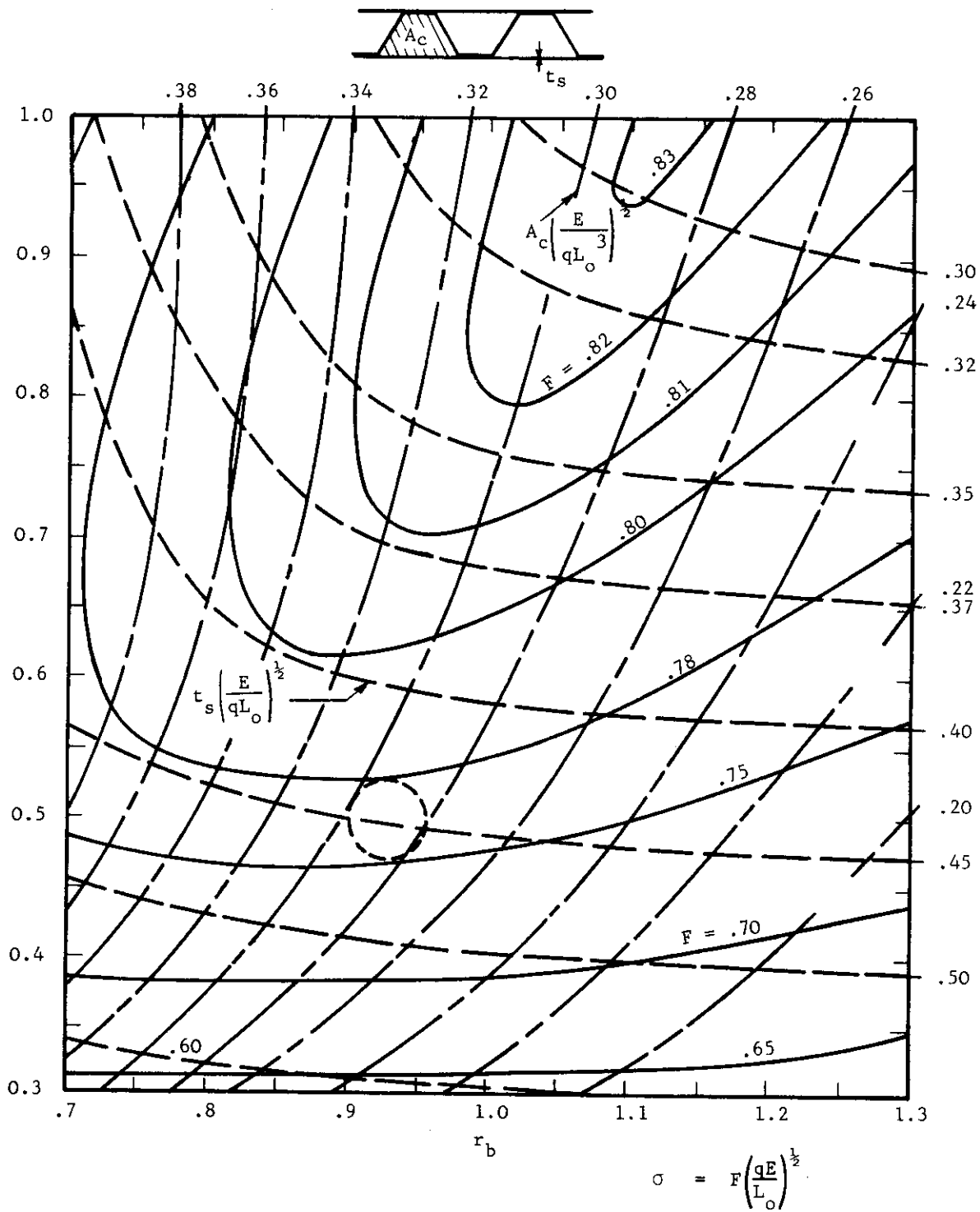


FIGURE 3. MINIMUM-WEIGHT DESIGN CHART FOR CORRUGATED CORE SANDWICH PANELS HAVING SKIN-GAGE AND CORE-PITCH CONSTRAINT, $r_A = 0.4$



S2135

FIGURE 4. MINIMUM-WEIGHT DESIGN CHART FOR CORRUGATED CORE SANDWICH PANELS
HAVING SKIN-GAGE AND CORE-AREA CONSTRAINT, $r_A = 0.4$

and the maximum attainable stress level can be computed as

$$\sigma = F \left(\frac{qE}{L_o} \right)^{\frac{1}{2}} = 0.76 \left[40(10.5)(10^6) \right]^{\frac{1}{2}} = 15,600 \text{ lb/in}^2 \quad (11)$$

The above design data in conjunction with the specified constraints, $t_s = 0.043$ inch and $b_s = 1.48$ inch, enable the complete definition of the shell cross-section. The additional dimensions of the cross-section are given below.

$$t_w = r_t(t_s) = 0.0215 \text{ inch}$$

$$b_w = r_b(b_s) = 1.38 \text{ inch}$$

$$b_A = r_A(b_s) = 0.59 \text{ inch}$$

$$\phi = \cos^{-1} \frac{b_s - b_A}{2b_w} = 71 \text{ degrees}$$

SECTION 3

EXPERIMENTAL PROGRAM

3.1 GENERAL CONSIDERATIONS

The experimental program was conducted in two phases. The first phase of the program was directed toward substantiating the design techniques developed in Reference 1 for wide columns. The second phase consisted, primarily, of a demonstration of the integrity of a representative cylindrical structure.

In the first phase of the test program, four wide column specimens were fabricated and tested. Two of the specimens had the same cross-section proportions as the double-wall shell designed in Section 2, and these were tested at the same structural index, $q/L_0 = 40$, used in the shell design. The other two wide column specimens were also tested at $q/L_0 = 40$; however, the cross-section proportions of these specimens were changed considerably.

In the second phase of the experimental program, five cylindrical double-wall shells were tested under axial load with, and without, internal pressure. The primary purpose of the cylindrical shell tests was to demonstrate the integrity of a representative structure. For purposes of this demonstration, three cylindrical shells having the same cross-section proportions as the double-wall shell designed in Section 2 were tested at the design $q/L_0 = 40$. One cylinder in this set of three was tested under axial load alone, while the other two were tested under an axial load combined with an internal pressure of 15 psig. The remaining set of two cylinders were tested at the design $q/L_0 = 40$; but, as in the case of the wide columns, the cross-section proportions of these cylinders were changed considerably.

The reason for including in the test program wide-columns and cylinders having cross-section proportions considerably different from those of the generated design was to study the effect of local buckling on the ultimate load. The proportions of the elements making up the cross-section of the design generated in Section 2 were such that local buckling was initiated in the core elements prior to the ultimate load. This manner of buckling is predicted by Figure 6-5 of Reference 1. That is, for designs of these proportions the facing sheet is called upon to restrain the buckling of core.

Another possibility of local buckling exists for certain minimum-weight designs. In meeting some combinations of the constraint parameters, it is possible for the double-wall design to fall within the upper region on Figure 6-5 (Ref. 1). In the region, above the dashed line, the facing sheet buckles first and the core is called upon to restrain the buckling of the facing sheet. Therefore, in order to assure that this latter possibility in design would not introduce unforeseen peculiarities of failure, the additional specimens were purposely proportioned so as to fall within this region of interest. As a means of identifying the two cross-section types employed in the test program, "70° core" refers to the design generated in Section 2 and "45° core" refers to the design included for study of the effect of local buckling.

3.2 WIDE COLUMN TEST PROGRAM

a. Test Specimens

Four wide columns, two having a 70° corrugated core and two having a 45° corrugated core, were fabricated from 2024-T3 aluminum alloy sheet for the initial phase of the test program. The cross-sections of the two wide columns having a 70° corrugated core were proportional to that of the representative double-wall shell given in Section 2.4. The dimensions of the full-scale cross-section were scaled down proportionately by a factor of 2.17 and then fabricated as close as possible to these reduced dimensions.

For purposes of fabricating and testing representative specimens, it was expedient to reduce the size of the full-scale cross-section by approximately a factor of 2. However, in keeping the sheet thicknesses to standard sizes, a reduction-factor of 2.15 was found necessary. This value was, then, further adjusted to 2.17 which served as a compromise in the detail design of the cylindrical specimens to be fabricated later. The curvature of a cylindrical double-wall shell necessarily produces a slight expansion and contraction of the corrugation pitch at the outer and inner surfaces, respectively.

The "as fabricated" cross-sections of the double-wall wide columns and the cylindrical specimens are shown in Figure 5. The dimensions listed correspond to the average measurements taken from both the wide column and cylindrical specimens. The facing sheets and corrugated core were adhesive bonded as per MIL-A-8431, Type 1.

The four wide column specimens were fabricated with the grain direction of both the skin and core sheet material oriented in the transverse direction.

Another important consideration in the fabrication of the specimens was in the specification of the wide-column length to be used in the tests. In order for results obtained from a wide-column specimen having a scaled-down cross-section to be representative of the full-scale structure, the effective length, L_0 , must be scaled down by the same factor. The effective length of the full-scale double-wall shell was shown to be 48.8 inches (see Section 2.1). Therefore, by applying the scale factor, the required effective length of the test specimens was computed to be $48.8 / 2.17 = 22.5$ inches.

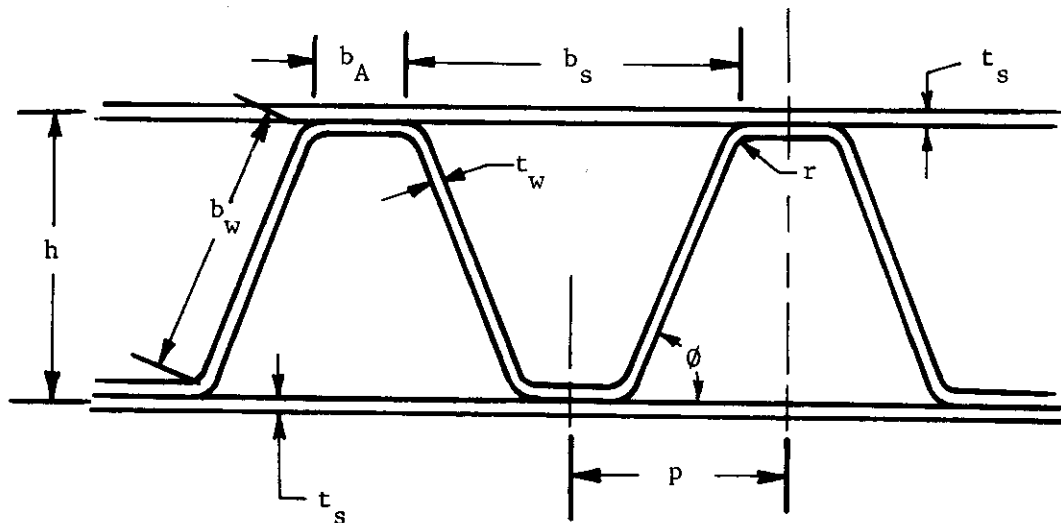
For wide columns having ends machined flat and parallel and carefully aligned in the testing machine, an end fixity coefficient very nearly equal to 4.0 has been indicated (Refs. 3, 4, and 5), and this value was used to determine the actual fabricated length of the specimens. The fabricated length became $22.5 \times \sqrt{4} = 45.0$ inches. Before the final machining, the ends of each specimen were filled to a depth of $1\frac{1}{2}$ inches with a hard plastic-like material (Epon 828 - Polyamide 115). This procedure of preparing the ends of the specimens is standard practice, although Cerrobend is often used in place of the plastic filler.

The width of the wide columns was not a critical dimension. The average widths of the 70° and 45° corrugated core specimens were 16.4 and 17.4 inches, respectively.

Typical material properties for the 2024-T3 aluminum alloy sheet were used in reducing the data. The modulus of elasticity, E , was taken as $10.5(10^6)$ lb/in² and Poisson's ratio, μ , was assumed to be $1/3$.

b. Test Procedure

The wide column specimens were loaded in axial compression in a 300,000-pound capacity screw-power testing machine. The specimens were carefully aligned in the testing machine to insure uniform loading through the platens of the testing machine. The specimens were tested as columns without side support.



$\phi = 70^\circ$	$\phi = 45^\circ$
$p = .48$ inches	$p = .85$ inches
$h = .65$ "	$h = .65$ "
$b_A = .27$ "	$b_A = .25$ "
$b_s = .68$ "	$b_s = 1.45$ "
$b_w = .65$ "	$b_w = .85$ "
$t_s = .020$ "	$t_s = .020$ "
$t_w = .010$ "	$t_w = .020$ "
$r = .030$ "	$r = .060$ "

$$r_A = \frac{b_A}{b_s}$$

$$r_b = \frac{b_w}{b_s}$$

$$r_t = \frac{t_w}{t_s}$$

S 2136

FIGURE 5. SECTION DETAILS OF CORRUGATED-CORE SANDWICH PANELS AND CYLINDERS

Each of the four wide column specimens was instrumented with resistance-type, paper base, bonded wire strain gages. On each specimen four 13/16 inch nominal gage-length gages were used to detect local buckling of the facing sheet between corrugations, and one 6-inch nominal gage-length gage was used to detect general buckling and to indicate the stress-strain relationship of the specimen. In addition, the column end-shortening was measured throughout the tests with dial gages sensing the movement of the upper loading platen.

Figure 6 shows one of the two 45° corrugated core specimens loaded very near the ultimate load. The location of the strain gage instrumentation is clearly shown. Two additional 13/16 inch gages are mounted on the far side of the specimen.

Loads were applied very slowly to specimens with a short pause at the end of each load increment to make the manual recordings of strain. The load increments were not uniform throughout the test. Readings were taken at large load intervals at the beginning of the test and at very short intervals as the ultimate load was approached.

c. Results and Discussion

The comparison of the theoretical and experimental efficiencies obtained for the 70° and 45° corrugated core specimens is shown in Figure 7. The relationships shown in this figure between F , q/L_0 , and L_0/A_1 were determined from the "maximum-stress" equation for minimum-weight wide columns,

$$\sigma = F \left(\frac{qE}{L_0} \right)^{\frac{1}{2}} \quad (12)$$

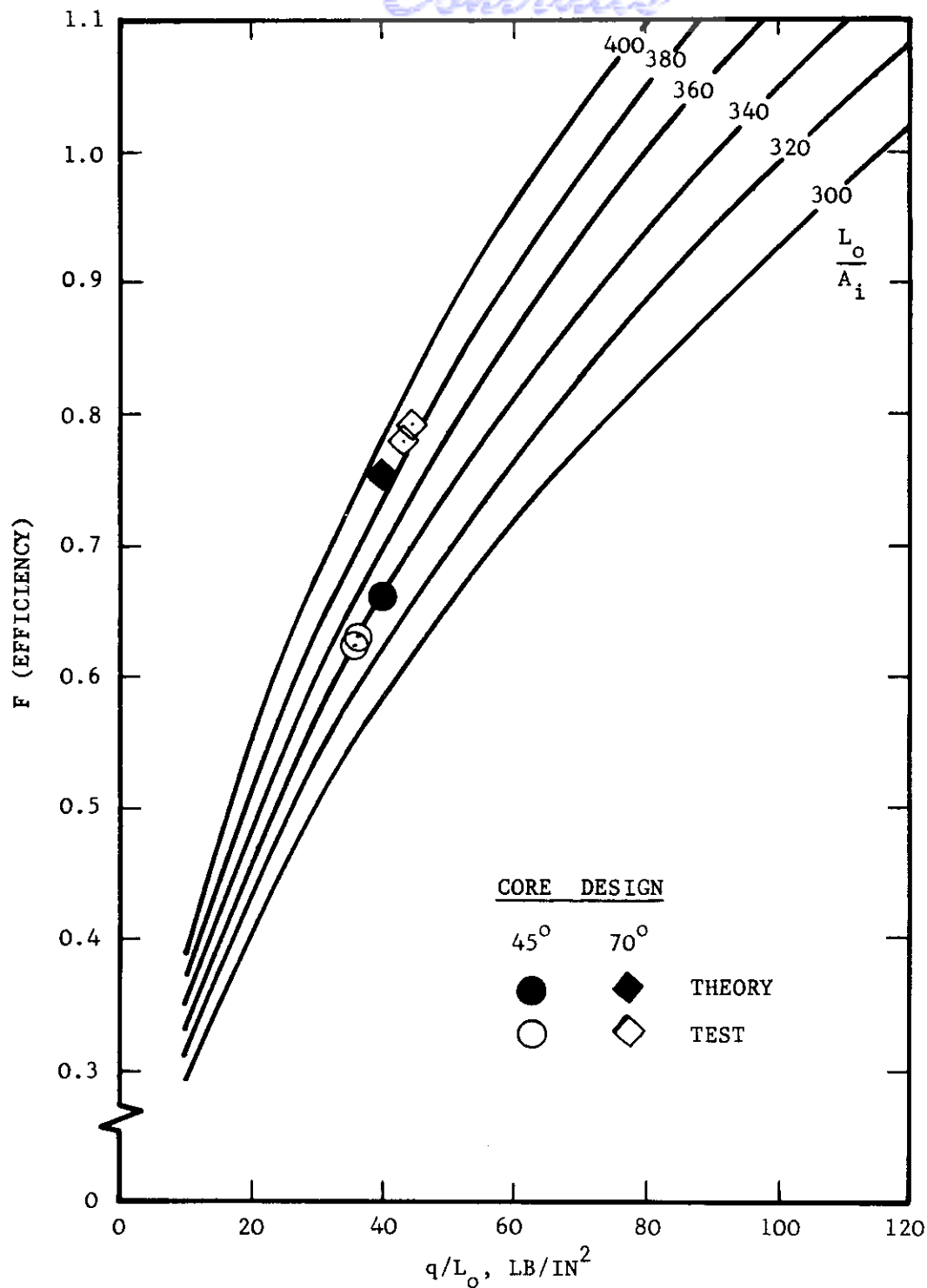
By solving Equation (12) for the structural efficiency, F , and replacing the maximum attainable stress, σ , with its equivalent, q/A_1 , gives

$$F = \frac{q/A_1}{(q/L_0)^{\frac{1}{2}} E^{\frac{1}{2}}} \quad (13)$$

This equation is put into the final required form by multiplying the numerator and denominator by $L_0^{\frac{1}{2}}$ and re-arranging. The resulting relationship is



FIGURE 6. TYPICAL TEST SET-UP AND LOADING OF WIDE COLUMNS



S2138

FIGURE 7. COMPARISON OF THEORETICAL AND EXPERIMENTAL EFFICIENCIES OF TWO ALUMINUM ALLOY WIDE-COLUMN DESIGNS

$$F = \left(\frac{q}{L_o} \right)^{\frac{1}{2}} \left(\frac{L_o}{A_i} \right) \left(\frac{1}{E} \right)^{\frac{1}{2}} \quad (14)$$

where

$$\frac{L_o}{A_i} = \frac{L_o}{t_s \left(\frac{A_i}{t_s} \right)}$$

The theoretical points on Figure 7 are determined by setting $q/L_o = 40 \text{ lb/in}^2$, $E = 10.5(10^6) \text{ lb/in}^2$, and using the design value for L_o/A_i . The relation, A_i/t_s , used in solving for L_o/A_i can be found in Appendix A.

The experimental points on Figure 7 are determined using the same design value for L_o/A_i , however, the test value of q/L_o is found from the relationship

$$(q/L_o)_{\text{test}} = \frac{P/b}{L_o} \quad (15)$$

where $P = \text{maximum test load, lb}$
 $b = \text{column width, inches}$
 $L_o = L/\sqrt{C} = 22.5 \text{ inches}$

The physical picture that should be obtained from Figure 7 is that the application of increasing loads to a given specimen produces a movement along a line corresponding to a constant value of L_o/A_i . That is, during the test q/L_o and F increase in value, reaching a peak at the ultimate load.

The agreement shown in the figure between the theoretical and experimental efficiencies is very good. Based on efficiency the 70° and 45° corrugated core wide columns were, respectively, under estimated by 5 percent and over estimated by 6 percent.

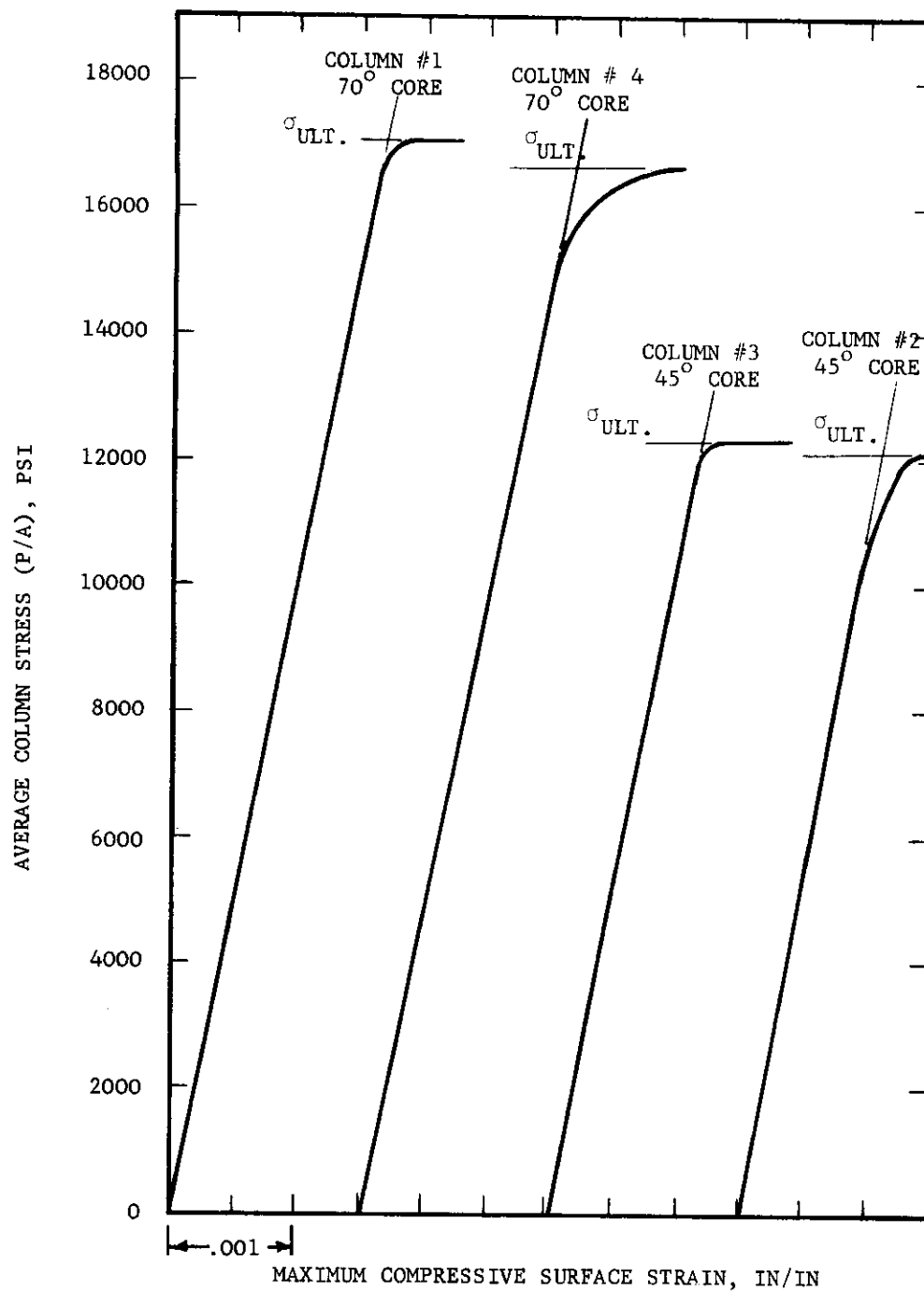
As discussed earlier in Section 3.1, the two designs considered here had proportions such that local buckling was initiated in the corrugated core of the 70° design and in the facing sheet of the 45° design. (See Figure 6 for the latter case.) The initial buckling of the facing sheet on the 45° core specimens appears to have contributed to the slightly unconservative results found for these designs. Although local buckling of the facing sheet would be expected to have a greater effect on the general instability of the column than the local buckling of the flat elements of the corrugations, the magnitude of the effect was not large.

The stress-strain relationships for the wide-column specimens are shown in Figure 8. The strains shown are those encountered by the 6-inch strain gage on the concave side of the general instability mode of the specimen. The end-shortening of the specimens was also recorded. The data obtained indicated that in each case the load versus end-shortening remained linear (elastic) up to the last data point recorded which was just short of ultimate load.

3.3 CYLINDRICAL SHELL TEST PROGRAM

a. Test Specimens

Five cylindrical, double-wall, shells were tested in this final phase of the experimental program. Three of the cylinders were fabricated with a cross-section and diameter proportional to that of the representative double-wall shell given in Section 2.4. The other two cylinders were fabricated with cross-section dimensions as close as possible to those of the 45°, corrugated-core, wide column specimens discussed in the foregoing section. The section details listed in Figure 5 correspond to the average measurements of the fabricated specimens. The curvature of the cylindrical shell necessarily produces a slight expansion of the corrugation pitch at the outer skin and a contraction at the inner skin. However, the dimensions as measured at the inner and outer radius were averaged and the average values were found to vary insignificantly from those listed in Figure 5. All dimensions, except length, of the 70° core cylinders were scaled down from the full-scale structure by a factor of 2.17. The selection of this factor was discussed in Section 3.2.a. The 45° core cylinders were then fabricated to the same diameter. As a result of applying the reduction factor to the 80-inch diameter of the full-scale structure, the outside diameter of the test cylinders became $80/2.17 = 36.9$ inches. The mean diameter was found to be 36.2 inches.



S2139

FIGURE 8. STRESS-STRAIN RELATIONSHIPS FOR
CORRUGATED CORE WIDE COLUMNS

The end fixity coefficient of the test cylinders was assumed to be the same as that of the wide-column specimens, namely 4.0. Therefore, as in the case of the wide-column specimens, the length of the cylinders necessary to give the same effective length as the full-scale shell was computed to be 45.0 inches. The ends of each cylinder were filled to a depth of $1\frac{1}{2}$ inches using the same plastic-like material (Epon 828 - Polyamide 115) employed on the flat specimens. The test cylinders were left in an open-ended condition with the ends machined flat and parallel for precise alignment in the testing machine.

The cylindrical shell specimens were fabricated from 2024-T3 aluminum alloy sheet with the grain direction of both the facing sheets and the corrugated sheet oriented in the circumferential direction. The adhesive bonding process used on the cylinders was the same as that employed with satisfactory results on the flat specimens. A single longitudinal splice was required in each facing sheet, and the resulting inner and outer splices were placed in diametrically opposite positions. The splice was achieved by butting the skin and overlapping this butt joint with a 4-inch wide longitudinal strip of 0.020 sheet. The two splice joints were also adhesive bonded as per MIL-A-8431, Type 1.

All test data on the cylinders were reduced using typical material properties for the 2024-T3 aluminum alloy sheet. The modulus of elasticity, E , and Poisson's ratio, μ , were assumed to be $10.5(10^6)$ lb/in² and $1/3$, respectively.

b. Test Procedure

Each of the cylindrical double-wall specimens was loaded in axial compression in the same 300,000-pound capacity screw power testing machine used in the wide-column tests. Figure 9 shows the typical positioning of a cylinder (without instrumentation) in the testing machine. The specimens were carefully aligned with the upper open-end in direct contact with the upper loading platen. The lower open-end of the cylinder was positioned on a thin sheet of galvanized metal comprising the bottom of a splash-box as shown in the figure. Although the splash-box was needed as a precautionary measure only during the tests on the pressurized cylinders, it remained in the machine throughout all cylinder tests. The upper loading platen was free to align itself to the upper end of the cylinder with the applied load passing through a standard spherically seated attachment.

Each of the five cylinders was instrumented with resistance-type, paper base, bonded wire strain gages. For the unpressurized test specimens the instrumentation consisted of six gages of 13/16 inch nominal

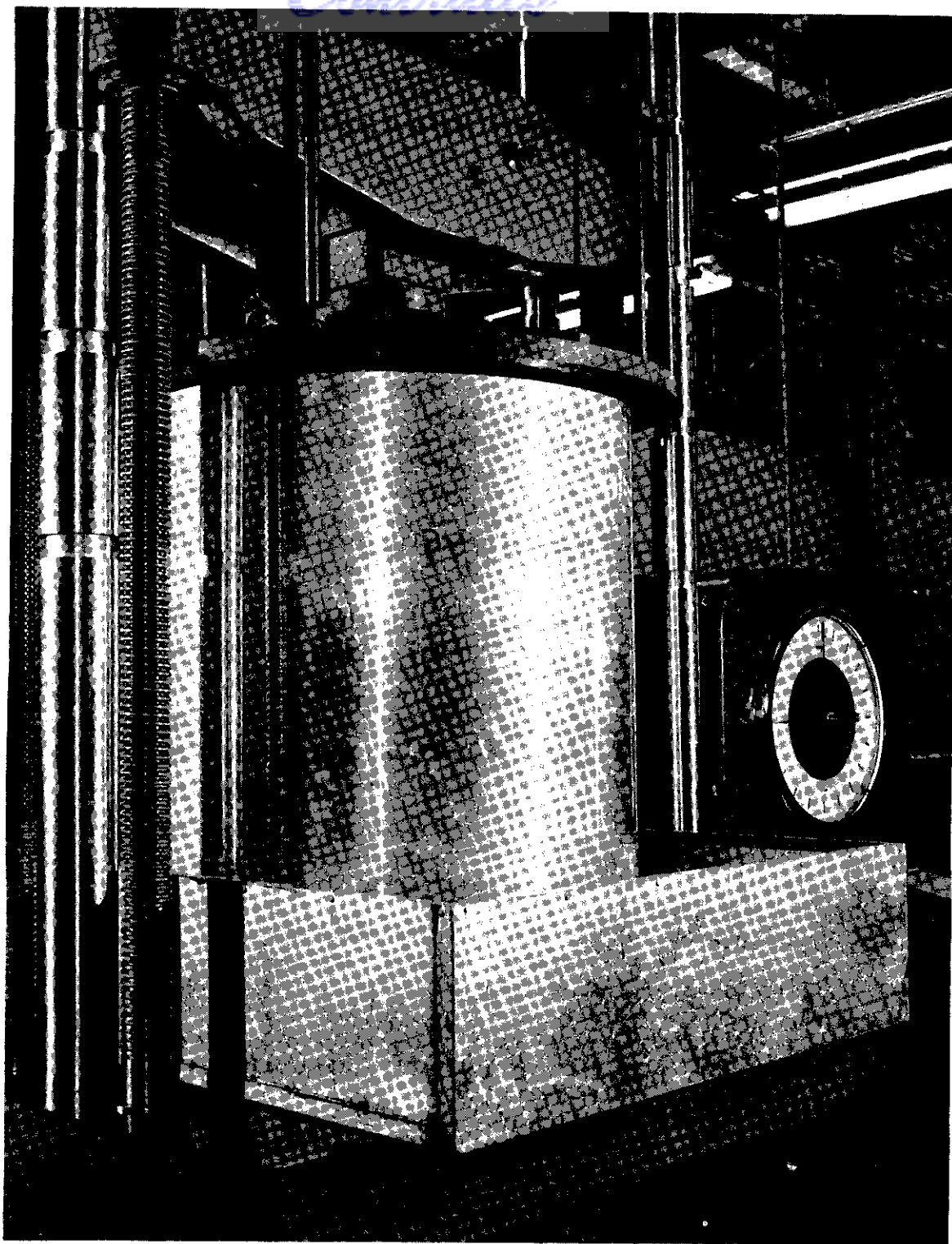


FIGURE 9. TYPICAL TEST SET-UP FOR CYLINDRICAL SHELLS

gage length and three gages of 6-inch nominal gage length. The shorter gages were mounted at three positions, 120° apart, on the inner and outer surfaces. These gages were used to detect local buckling of the inner and outer facing sheets between corrugations. The 6-inch gages were mounted 120° apart at mid-length of the outer surface. The longer gages were used to detect general buckling and to indicate the longitudinal stress-strain relationship of the specimen.

The pressurized cylinders were subjected to biaxial strains during the test, therefore the instrumentation on these cylinders was somewhat more extensive. In addition to the application of instrumentation identical to that of the unpressurized cylinders, the pressurized cylinders received two additional 6-inch gage-length gages and four 7/16 inch gage-length rosette gages (2 element-type). The additional 6-inch gages were mounted circumferentially, one on the inner surface and the other on the outer surface, for purposes of sensing the hoop-tension strains. The small, two-element, rosettes were also used for purposes of separating the hoop strains from longitudinal strains. Since water was used as a pressurizing medium, all internal gages and their lead wires were water-proofed with commercial water-resistant compounds.

The method of pressurization is shown in Figure 10. Access through the upper platen was provided at two pipe fittings, the left-hand one for filling with water and the right-hand one for applying air pressure. The necessary air pressure was supplied by means of standard line pressure passing through a sensitive regulator. Internal strain gage leads were brought to the outside through a pressure-tight fitting attached as a cap to the left-hand pipe fitting.

The procedure used in applying loads and recording data on the unpressurized cylinders was very similar to that used in the wide-column tests. That is, the loads were applied very slowly with readings being taken at large load intervals early in the test and at very short intervals as the load appeared to approach the ultimate.

The procedure of applying loads to the pressurized cylinders was somewhat more involved. After the cylinder was positioned and aligned, approximately 20,000 pounds of axial load was applied to seal the ends of the cylinder prior to filling with water. The water level was brought to within one inch of the upper platen and all strain gages were set to read a common initial value of 10,000 micro-inches per inch. The cylinder was then pressurized to 15 psig internal pressure (the space between the walls was vented to atmospheric pressure by means of a row of very small holes in the outer skin between each corrugation). No leaks were experienced in the tests, and the pressure held precisely. The pressure force

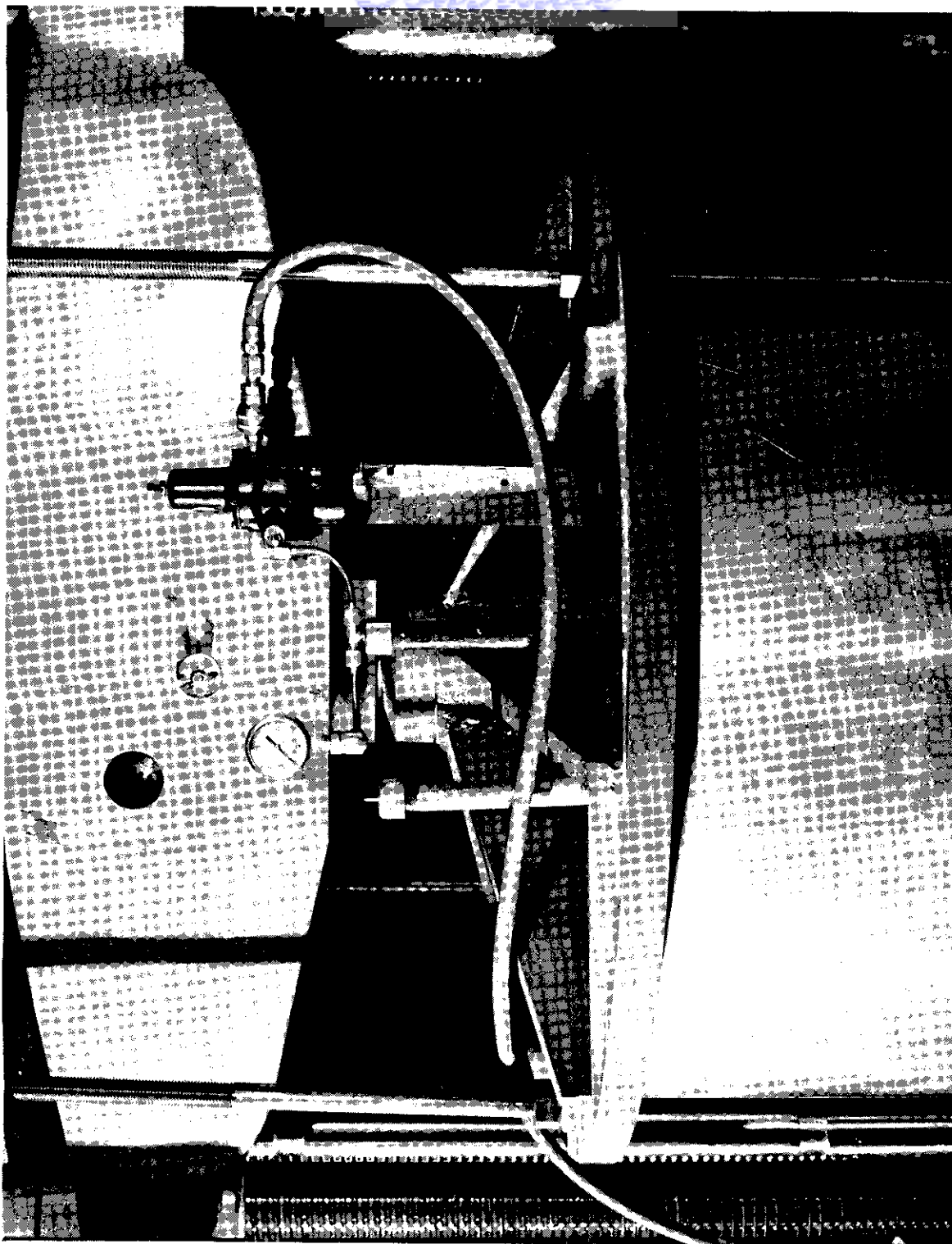


FIGURE 10. THE METHOD OF PRESSURIZING THE CYLINDRICAL SPECIMENS

tending to lift the upper platen was calculated to be $15(\pi)(35.5)^2/4 = 14,850$ lbs. This pressure force added to the water weight of 1600 lbs gave a value of 16,450 pounds acting against the weighing system of the testing machine. Therefore, this load had to be subtracted from each reading shown by the load indicator on the testing machine to give the true axial load exerted on the walls of the pressurized cylinder. After this initial procedure the application of load and recording of data did not differ from that of the unpressurized cylinders.

c. Results and Discussion

The stress-strain relationships for the two unpressurized cylinders (one cylinder of each cross-section) are shown in Figures 11 and 12. The axial strains shown are the average of the three 6-inch gages mounted at the mid-length of each cylinder. The critical buckling stress indicated on the figures is an average value determined from the local-buckling strains in the facing sheet as recorded from the six 13/16 inch gages. The axial load producing the local buckling of the skin was verified by observation. The non-linearity in the axial stress-strain relationship appeared to begin at the stress level corresponding to local buckling of the outer surface.

The design of the cross-section having the 70°-corrugated core was such that the facing-sheet was called upon to restrain the buckling of the core (see Section 3.1), whereas the design having the 45°-corrugated core had proportions which called upon the core to restrain buckling of the facing sheets. The latter case of local buckling is shown in Figure 13.

The stress-strain relationships for the three pressurized cylinders are shown in Figures 14, 15, and 16. The results obtained from strain gages mounted on the inner and outer surface are shown in the latter figures. The strain-gages located on the inner surface of cylinder #2 (70° core) shorted out during the test; therefore, only outer skin measurements are presented for this specimen. The short was traced to faulty water-proofing of the gage lead-wires and by improving the water-proofing technique these failures did not re-occur during the subsequent cylinder tests.

In reducing the strain-gage data composed of both axial and transverse (hoop) strains the following relationships for the biaxial stresses were employed,

$$\sigma_{\text{axial}} = \frac{E}{1 - \mu^2} (\epsilon_L + \mu\epsilon_T) \quad (16)$$

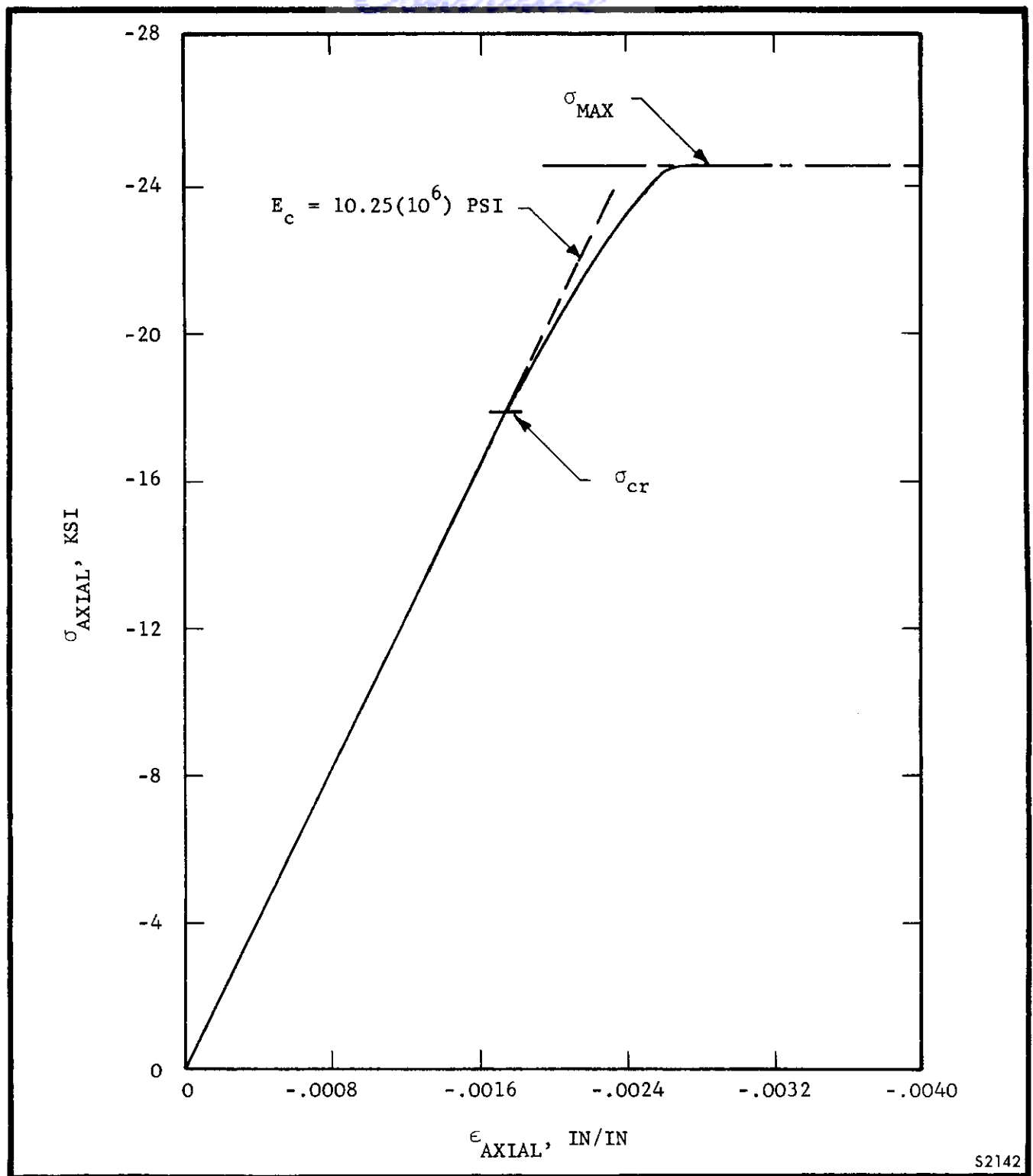
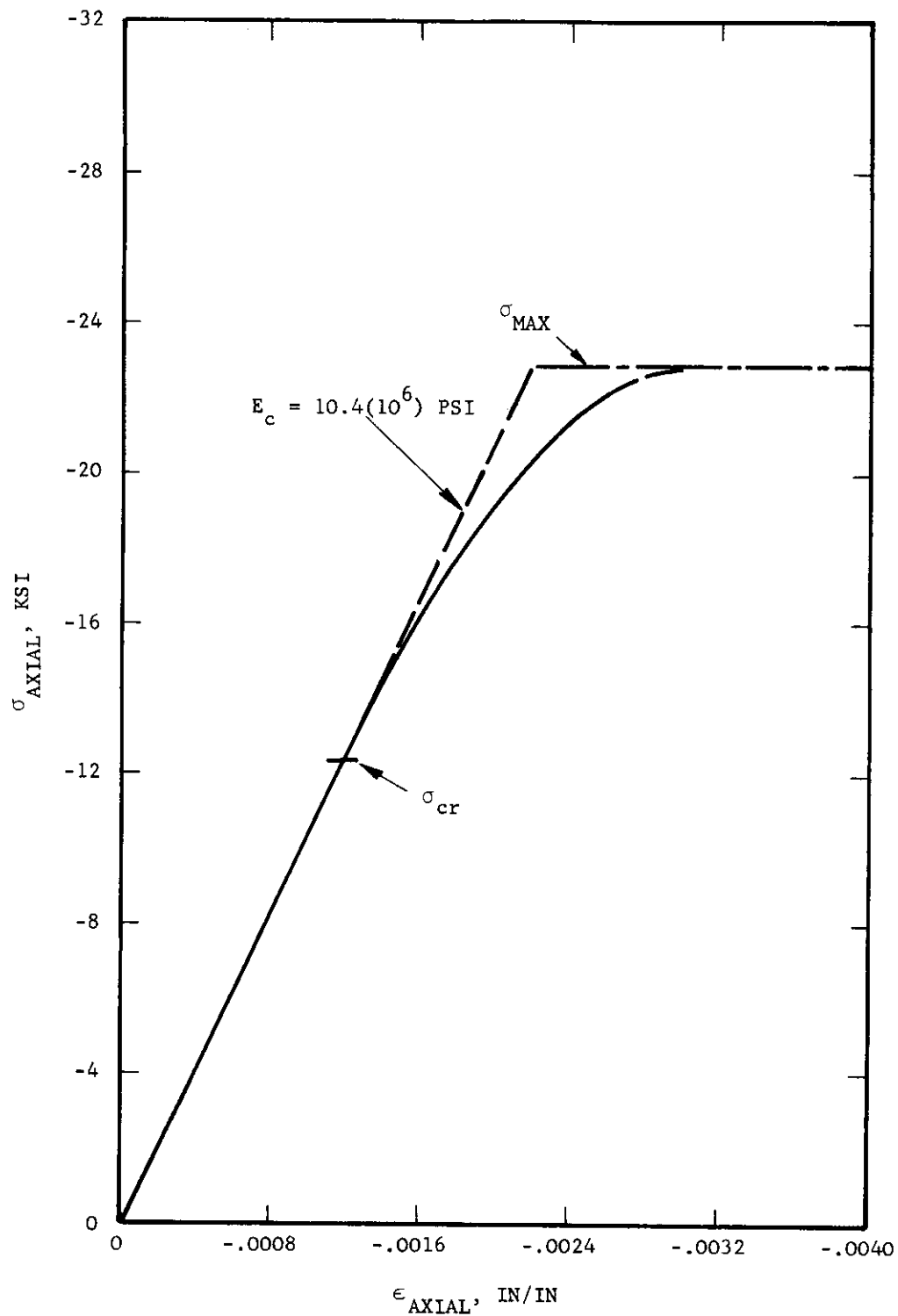


FIGURE 11. STRESS-STRAIN RELATIONSHIP FOR UNPRESSURIZED CYLINDER #1, (WALL SECTION - 70° CORE)



S2143

FIGURE 12. STRESS-STRAIN RELATIONSHIP FOR UNPRESSURIZED CYLINDER #4 (WALL SECTION - 45° CORE)

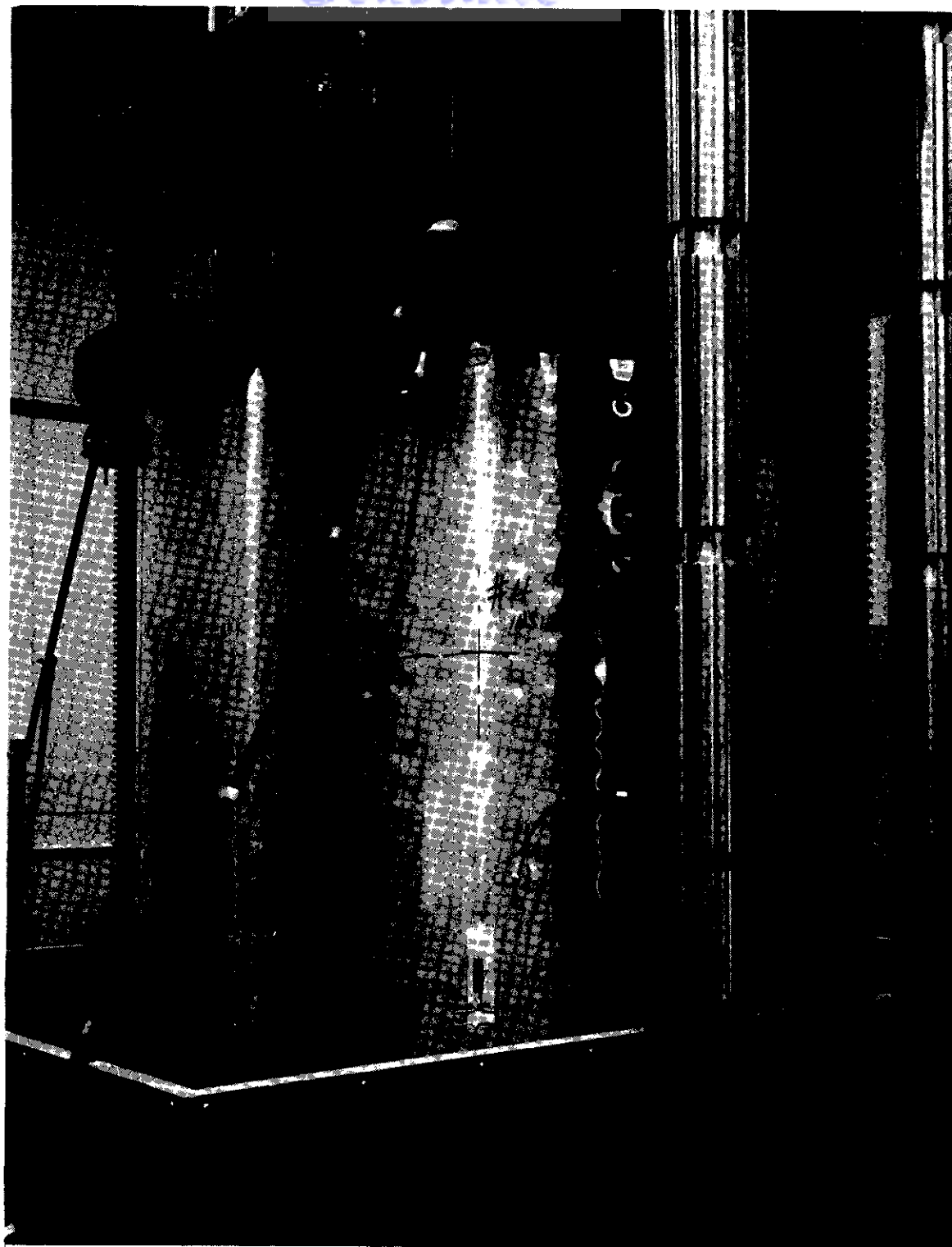
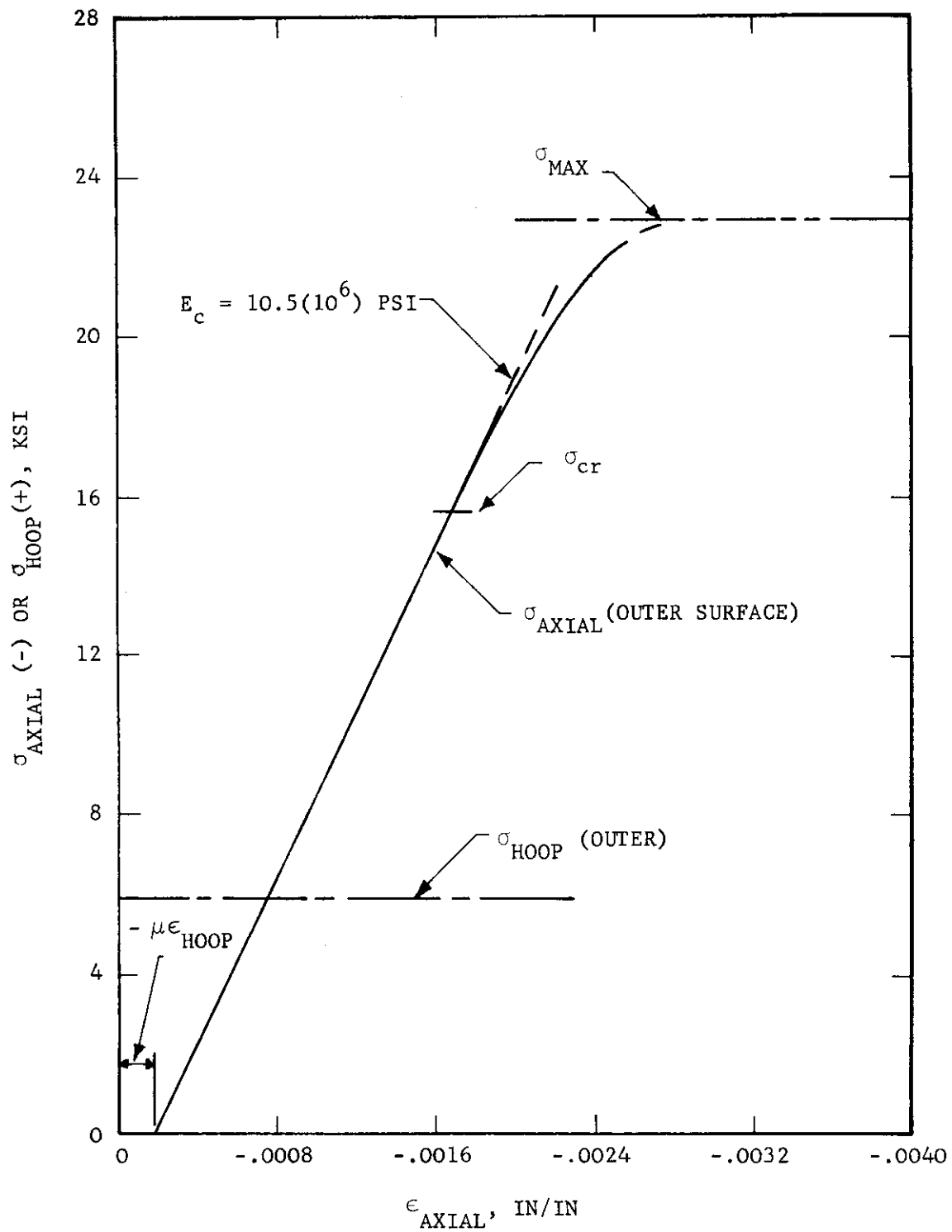
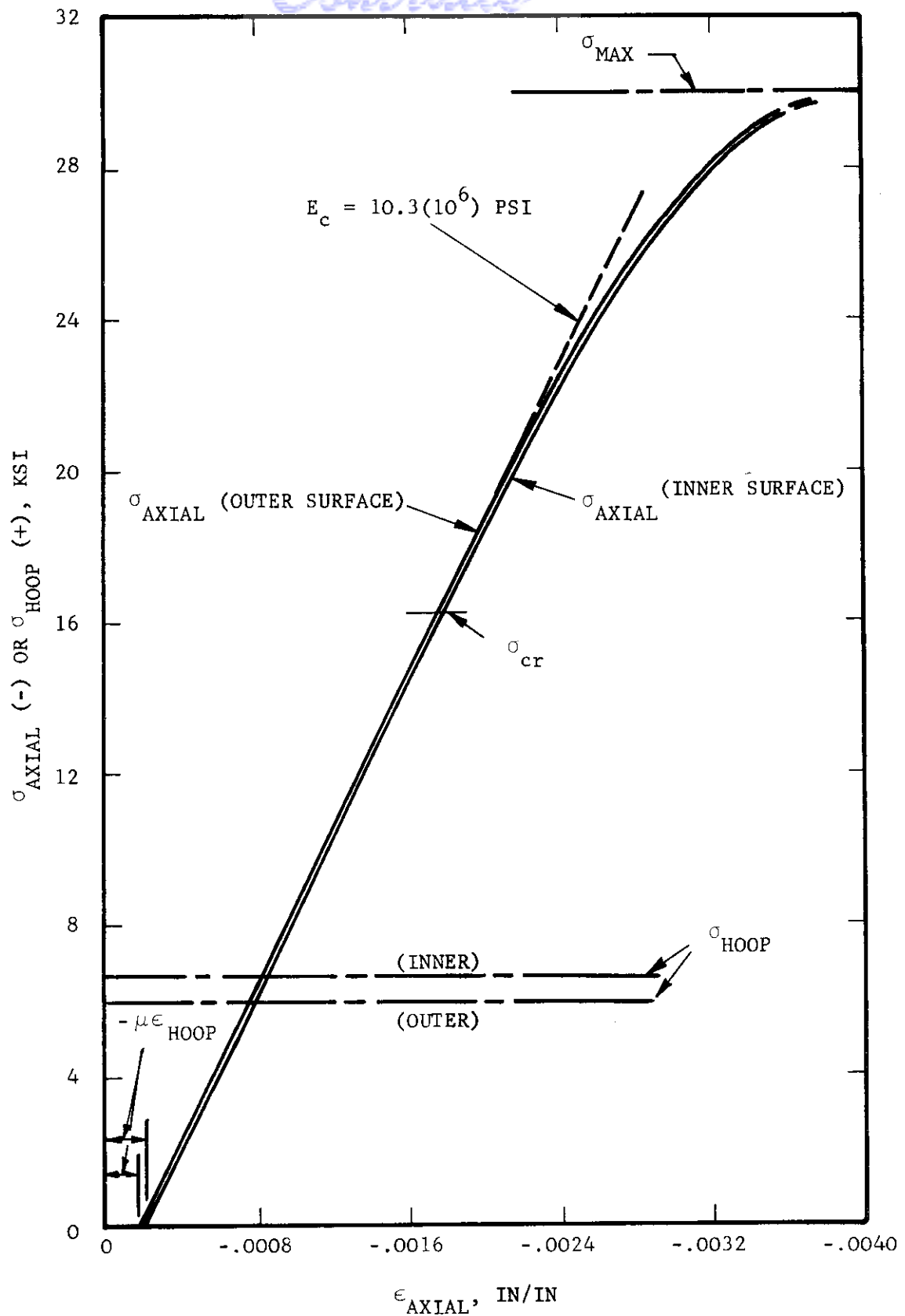


FIGURE 13. LOCAL BUCKLING DISPLAYED BY CYLINDER
HAVING 45° -CORRUGATED CORE



S2145

FIGURE 14. STRESS-STRAIN RELATIONSHIPS FOR PRESSURIZED CYLINDER #2 (WALL SECTION - 70° CORE)



52146

FIGURE 15. STRESS-STRAIN RELATIONSHIPS FOR PRESSURIZED CYLINDER #3 (WALL SECTION -70° CORE)

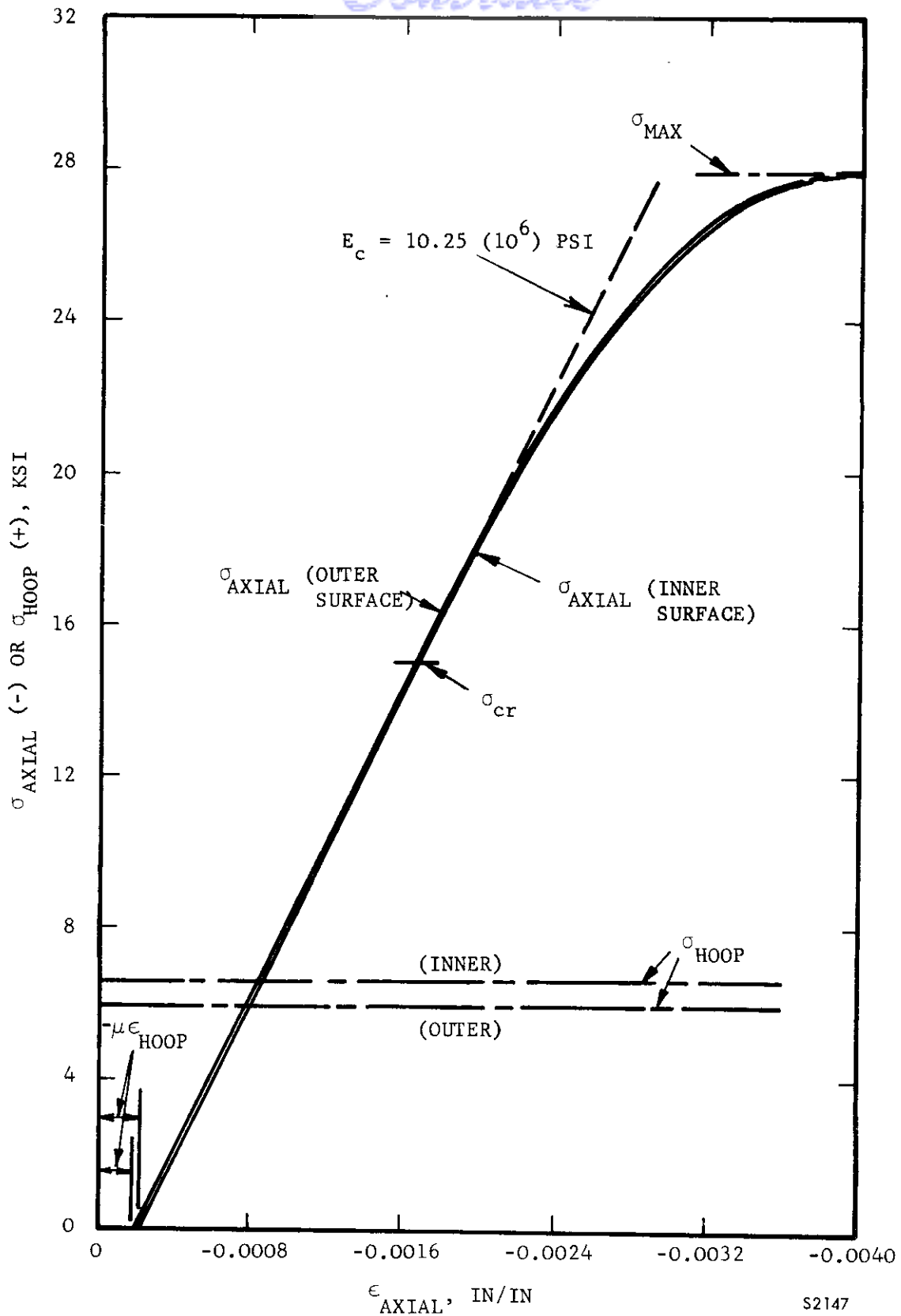


FIGURE 16. STRESS-STRAIN RELATIONSHIPS FOR PRESSURIZED CYLINDER #5 (Wall Section - 45° Core)

$$\sigma_{\text{hoop}} = \frac{E}{1 - \mu} (\epsilon_T + \mu \epsilon_L) \quad (17)$$

where, ϵ_L and ϵ_T are the recorded strains in longitudinal and transverse directions, respectively.

The hoop tension stresses developed in the pressurized cylinders evidently affected the local-buckling stresses of the two types of cross-sections in different manners. By comparing the stress-strain curves for the pressurized and unpressurized cylinders, it can be observed that internal pressure had the effect of increasing the skin buckling stress for the 45°-core construction and decreasing this buckling stress for the 70°-core construction. These results appear to infer that the effect of internal pressure on the local buckling of double-wall construction is dependent on whether the facing sheets are restraining the core or vice versa.

The hoop-tension stresses did not vary significantly between the inner and outer skins nor between the type of core construction used for the cylinders. For most practical purposes the average hoop-tension stress between the inner and outer surfaces can be predicted by $\sigma = pR/t$, where the thickness, t , is the sum of the two facing sheet gauges. The internal pressure used in all pressurized cylinder tests was 15 psig, twice that considered as a minimum for the crew requirements of a representative space vehicle. Therefore, with the ratio R/t remaining constant between the full-scale vehicle and the test cylinders, the hoop-tension stress in the specimens is twice that expected to be encountered by the full-scale shell.

The mode of failure that was found to be typical of all cylinders tested in this program is shown in Figure 17. In each case, just prior to the ultimate load, some snapping noises were quite audible, and at ultimate load a violent snap buckling occurred. The buckle pattern tended toward the diamond shape, with a circumferential wave length approximately two or three times that in the axial direction. For two of the cylinders the buckling mode shown in Figure 17 was accompanied in other regions of the cylinder by one or two circumferential wrinkles on the inner and outer surface. Failures very similar to those recorded here on longitudinally stiffened double-wall shells, were obtained in Reference 6 during a series of tests on several cylinders having walls fabricated of honeycomb sandwich materials.

In Figure 18 the recorded values of the residual strength (drop load) of each cylinder has been given. The importance of such remaining strength is questionable; however, since the values were easily obtained, they are included for completeness.

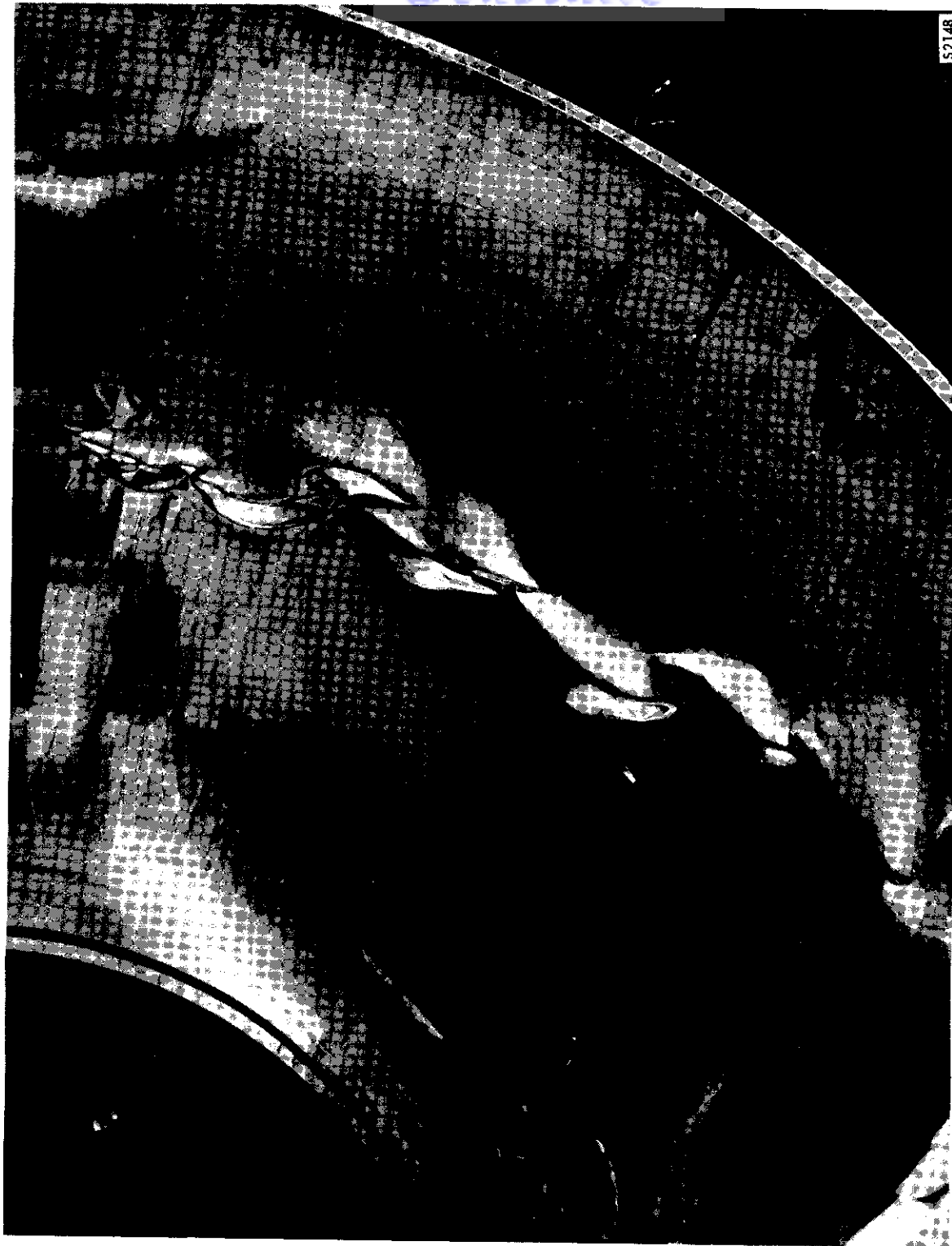


FIGURE 17. MODE OF FAILURE TYPICAL OF CYLINDERS

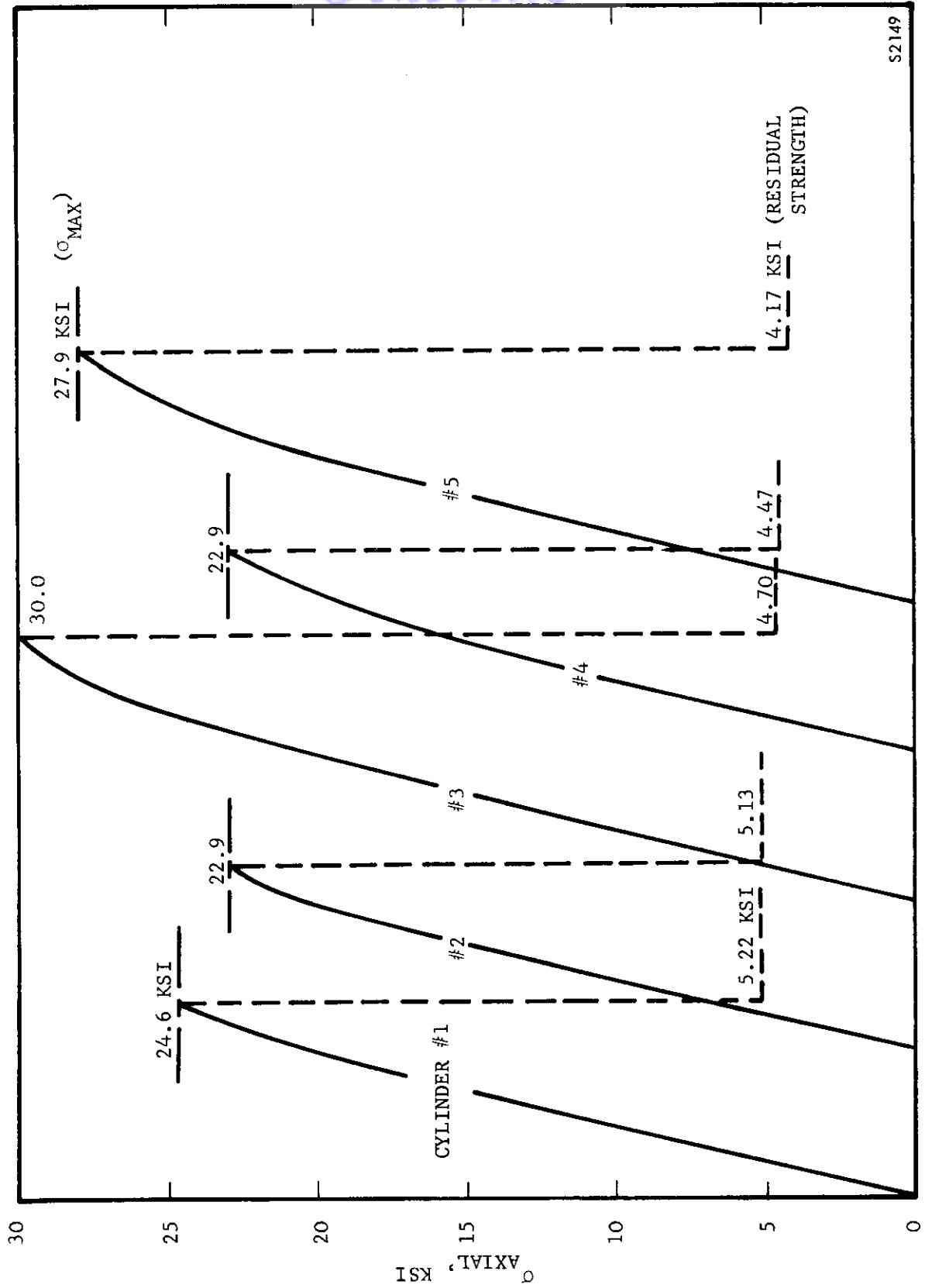


FIGURE 18. ULTIMATE AND RESIDUAL STRENGTHS OF CYLINDERS

The summary of all ultimate-load test results and a comparison of these with the theoretical predictions made through wide-column theory are shown in Figure 19. The wide-column results previously shown in Figure 7 have been re-presented for purposes of comparison with the cylindrical shell results. Again, as in Figure 7, the relationships presented in Figure 19 between F , q/L_0 and L_0/A_i were determined from the "maximum-stress" equation for minimum-weight, wide-column design. Equation (14) gives the final form of the relationships presented in the figure.

The experimental points for the cylinder tests are plotted at the intersection of the proper design value of L_0/A_i and the test value of q/L_0 . For the cylindrical shell specimens the test value of q/L_0 is found from the relationship,

$$(q/L_0)_{\text{test}} = \frac{P/\pi D_{\text{mean}}}{L_0} \quad (18)$$

where P = maximum axial load on cylinder, lb
 L_0 = L/\sqrt{c} = 22.5 inches
 D_{mean} = mean diameter = 36.2 inches

As expected, the theoretical efficiency determined through an application of wide-column theory offers a conservative estimate of the strength of cylindrical configurations. The higher efficiency displayed by the test cylinders is evidently associated with the strengthening effect of curvature in raising the general (or long-wave) buckling load of the shell wall. It has been common practice in minimum-weight design studies to avoid the analytical difficulties associated with the direct introduction of curvature effects. However, as can be observed from the results shown in Figure 19, the simplicity afforded by the wide-column approach is achieved only at the expense of some compromise of structural efficiency and some restrictions on optimization.

For the unpressurized cylinders having 45° and 70° corrugated cores, wide-column theory under-estimated the test efficiencies by 23 percent and 21 percent, respectively. Actually, however, these results may be considered very good if one reflects on the large disparity that exists between the orthotropic, shell-buckling theories and experiment for stiffened cylinders. Furthermore, the "more exact" shell theories generally require considerable modification through empirical correction factors before the errors of prediction can be reduced to nominal values.

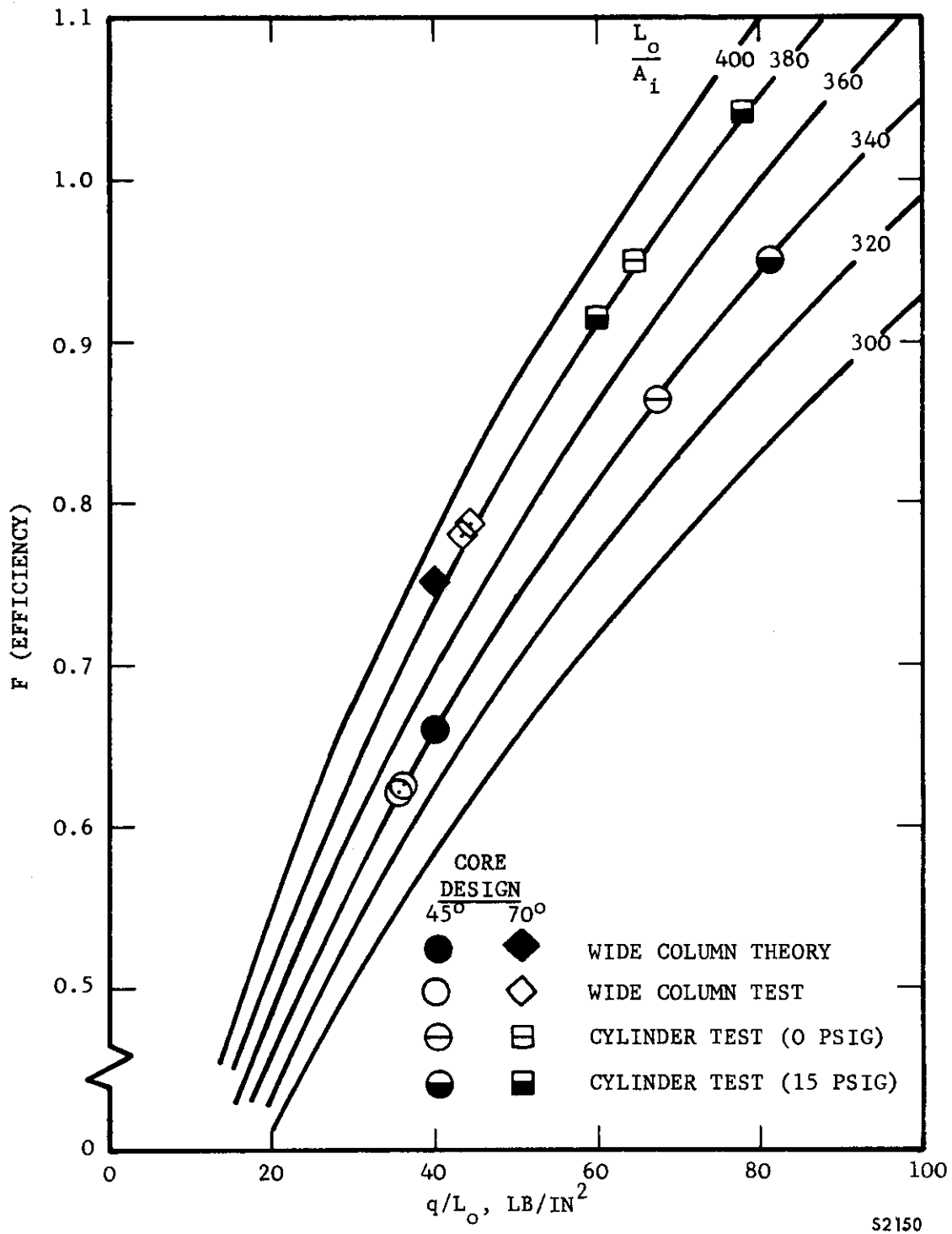


FIGURE 19. COMPARISON OF THE EFFICIENCY OF WIDE COLUMNS AND CYLINDERS HAVING IDENTICAL DOUBLE-WALL CROSS-SECTION

Contrails

From the limited number of specimens tested in this program it is difficult to reliably assess the effect of internal pressure on the strength of the cylindrical specimens. Other than the "lift off" effect of internal pressure in reducing the magnitude of the axial load applied to the cylinder, the strengthening effect on the cylinder wall is still in doubt. Of the two pressurized cylinders having a 70° corrugated core, one was found to carry a greater axial load while the other carried a lesser load than the unpressurized cylinder. Unfortunately, this scatter of the test results prevents the evaluation of the contribution of internal pressure for the 70°-core design. In the case of the cylinders having a 45° corrugated core, only one was available for test under pressure. This one test gave an efficiency 10½ percent higher than that of a similar unpressurized cylinder.

There does appear to be some benefit to the structural efficiency from internal pressurization at 15 psig. However, as pointed out in Reference 1, when the compressive loads reach peak values during the boost phase of a space vehicle trajectory, internal pressure cannot always be counted on for a structural stability effect. Depending upon the programming of the internal pressure during ascent, the peak resultant compressive load can occur well before the differential pressure across the shell wall reaches a significant level.

The residual strength recorded for each cylinder has been previously given in Figure 18. At failure and during the strength-drop exhibited in the figure, the pressurized cylinders (Nos. 2, 3, and 5) displayed very good "fail-safe" characteristics. That is, although the failures of the pressurized cylinders were characterized by a violent form of snap buckling producing severe damage to both inner and outer facing sheets as well as corrugated core, there was no tendency toward the explosive-decompression type of failure. In fact, at the drop loads or residual strengths shown in Figure 18, the internal pressure was maintained without leakage through the double-wall or the cylinder-ends in contact with the loading platens.

The pressurized cylinders carried hoop tension stresses of approximately 6.6 and 5.9 ksi in the inner and outer skins, respectively. Even though these levels of stress are twice that expected in the skins of a full-scale representative structure, the stresses are still quite low. Hoop-stress levels of this magnitude will require critical crack lengths at least two to three feet long before catastrophic failures are imminent in a typical double-wall shell. Critical crack lengths for pressurized unstiffened cylinders were studied in Reference 7 using the same 2024-T3 aluminum alloy employed in the present program. By applying the conservative methods of Reference 7 to the full-scale dimensions of a representative space structure,

critical crack length as a function of hoop stress was calculated. The results of these computations are shown in Figure 20 for an unstiffened cylinder. Even if the benefit of stiffening through double-wall construction is neglected, a hoop tension stress of 3.3 ksi (full-scale vehicle having 7.5 psi internal pressure) requires a critical crack length in excess of 35 inches. If one facing sheet were to fail completely and the stress in the other sheet were to double, the critical crack length is found to be approximately 22 inches. This latter possibility is shown by the horizontal line near the right end of the curve in Figure 20.

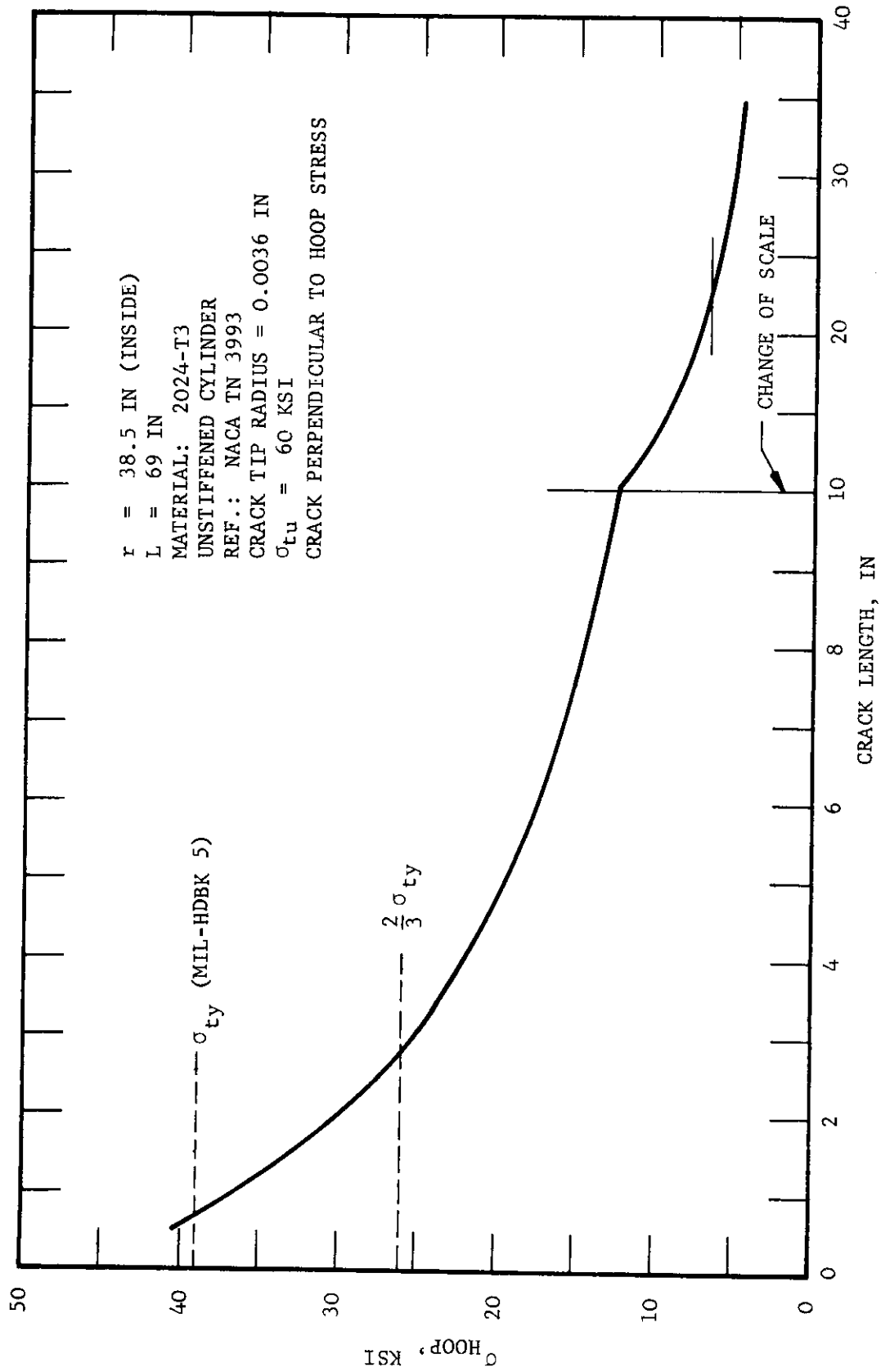


FIGURE 20. CRITICAL CRACK LENGTH FOR A PRESSURIZED UNSTIFFENED CYLINDER S2151

SECTION 4

CONCLUSIONS

The agreement found in this study between the theoretical and experimental efficiencies of double-wall wide columns having a corrugated-core cross-section is very good. Therefore, the minimum-weight design procedures presented in Reference 1 and discussed in this report appear to offer an accurate means of establishing the structural efficiencies of double-wall wide columns. The efficiency predictions were not significantly affected by the location of local buckling in the cross-section. That is, local buckling initiated in either the core or facing sheet had little effect on the accuracy of the predictions.

The test results on the double-wall cylindrical shells indicate that the effect of internal pressure on the local buckling of the cross-section is dependent on whether the facing sheets are restraining the core or the core is restraining the facing sheets.

The theoretical efficiency, determined through an application of wide-column theory offers a conservative estimate of the strength of cylindrical, double-wall shells. The increased efficiency displayed by the cylindrical, double-wall specimens appears to be associated with the strengthening effect of curvature in raising the general buckling load of the shell wall.

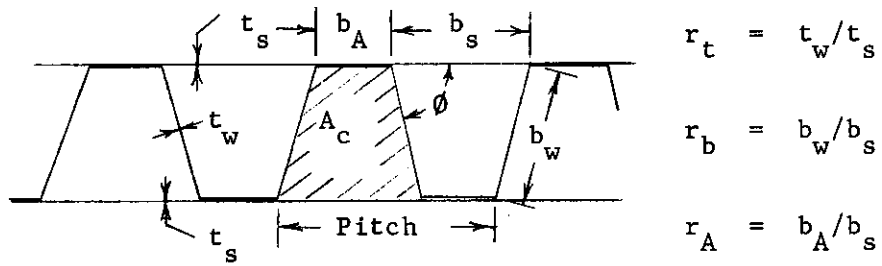
The simplicity afforded by using the wide-column approach on cylindrical shells is achieved at the expense of some compromise of the structural efficiency. For the unpressurized cylinders tested, the wide-column theory underestimated the test efficiencies by approximately 22 percent. However, these results may be considered good if one reflects on the large disparity that exists between the orthotropic, shell-buckling theories and experiment for stiffened cylinders.

REFERENCES

1. Lampert, S. and Younger, D. G., "Multi-Wall Structures for Space Vehicles," WADD TR 60-503, May 1960.
2. Janssen, J. E., "Thermal Comfort in Space Vehicles," ASME Paper 59A-207, 1959.
3. Schuette, E. H., Barab, S. and McCracken, H. L., "Compressive Strength of 24S-T Aluminum-Alloy Flat Panels with Longitudinal Formed Hat-Section Stiffeners," NACA TN 1157, 1946.
4. Dow, N. F. and Hickman, W. A., "Design Charts for Flat Compression Panels Having Longitudinal Extruded Y-Section Stiffeners and Comparison with Panels Having Formed Z-Section Stiffeners," NACA TN 1389, 1947.
5. Dow, N. F. and Hickman, W. A., "Data on the Compressive Strength of 75S-T6 Aluminum-Alloy Flat Panels with Longitudinal Extruded Z-Section Stiffeners," NACA TN 1829, 1949.
6. Kazimi, M. I., "Sandwich Cylinders - Part II: Uniformity of The Mechanical Properties of the Core," Aerospace Engineering, Vol. 19, No. 9, September, 1960.
7. Peters, R. W. and Kuhn, P., "Bursting Strength of Unstiffened Pressure Cylinders with Slits," NACA TN 3993, April 1957.

APPENDIX A

GEOMETRICAL RELATIONSHIPS FOR CORRUGATED CORE DOUBLE-WALL CONSTRUCTION



A.1 CROSS-SECTION PROPERTIES

$$\frac{A_i}{t_s} = \frac{2 (r_b r_t + r_A r_t + r_A + 1)}{1 + r_A} \quad (A-1)$$

$$I_{pitch} = \frac{1}{24} t_s b_s^3 \left[4r_b^2 - (1 - r_A)^2 \right] \left[r_b r_t + 3(r_A r_t + r_A + 1) \right] \quad (A-2)$$

$$A_{pitch} = 2 t_s b_s (r_b r_t + r_A r_t + r_A + 1) \quad (A-3)$$

$$\rho^2 = \frac{b_s^2}{48} \frac{\left[4r_b^2 - (1 - r_A)^2 \right] \left[r_b r_t + 3(r_A r_t + r_A + 1) \right]}{(r_b r_t + r_A r_t + r_A + 1)} \quad (A-4)$$

$$\frac{\rho}{b_s} \frac{t_s}{A_i} = \frac{\sqrt{3} \left[4r_b^2 - (1 - r_A)^2 \right]^{\frac{1}{2}} \left[r_b r_t + 3(r_A r_t + r_A + 1) \right]^{\frac{1}{2}} (1 + r_A)}{24 (r_b r_t + r_A r_t + r_A + 1)^{3/2}} \quad (A-5)$$

A.2 STRUCTURAL EFFICIENCY RELATIONSHIP

$$F = 2.44 \left(\frac{K_x}{4} \right)^{\frac{1}{2}} \left(\frac{\rho}{b_s} \frac{t_s}{A_i} \right)^{\frac{1}{2}} \quad (A-6)$$

$$F = 0.657 \left(\frac{K_x}{4} \right)^{\frac{1}{2}} \frac{\left[4r_b^2 - (1 - r_A)^2 \right]^{\frac{1}{2}} \left[r_b r_t + 3(r_A r_t + r_A + 1) \right]^{\frac{1}{2}} (1 + r_A)^{\frac{1}{2}}}{(r_b r_t + r_A r_t + r_A + 1)^{3/4}} \quad (A-7)$$

where K_x is determined from Figure 6-5 of WADD TR 60-503 with $\theta = \cos^{-1}(1/2r_b)$.

A.3 DESIGN CONSTRAINT RELATIONSHIPS

$$t_s \left(\frac{E}{qL_o} \right)^{\frac{1}{2}} = \frac{0.50 (1 + r_A)}{F (r_b r_t + r_A r_t + r_A + 1)} \quad (A-8)$$

$$b_s \left(\frac{E}{qL_o^3} \right)^{\frac{1}{2}} = \frac{2.20F^{\frac{1}{2}} (r_b r_t + r_A r_t + r_A + 1)^{\frac{1}{2}}}{\left[4r_b^2 - (1 - r_A)^2 \right]^{\frac{1}{2}} \left[r_b r_t + 3(r_A r_t + r_A + 1) \right]^{\frac{1}{2}}} \quad (A-9)$$

$$A_c \left(\frac{E}{qL_o^3} \right)^{\frac{1}{2}} = \frac{1.21F (r_A + 1) (r_b r_t + r_A r_t + r_A + 1)}{\left[4r_b^2 - (1 - r_A)^2 \right]^{\frac{1}{2}} \left[r_b r_t + 3(r_A r_t + r_A + 1) \right]} \quad (A-10)$$

where the value of F in relationships (A-8), (A-9), and (A-10) is determined from relationship (A-7).

The relationships (A-7) through (A-10) have been plotted in Figures 3 and 4 of this report. In developing the curves presented, values of r_A , r_B , and r_t were selected and the corresponding values of the structural efficiency (F) and the three design constraint parameters were computed.

APPENDIX B

RELATIONSHIPS FOR METEOROID SHIELD DESIGN

In the development of Figure 1 the following parameters and equations were taken from WADD TR 60-503.

The expression for penetration depth can be written as

$$t_s = \frac{1.24 \gamma}{\left(\frac{1}{3} - \frac{\theta}{2}\right) \frac{\theta}{2}} \left(\frac{\rho_p}{\rho_T}\right)^{\left(\phi - \frac{1}{3}\right) \frac{1}{3}} m^{\frac{1}{3}} v^{\theta} \quad (B-1)$$

from which the meteoroid mass, m , capable of just penetrating a shield thickness, t_s , is obtained. The average number of particles $\bar{N}_>$ having masses equal to or less than m is found from the relation

$$\bar{N}_> = \alpha m^{-\beta} A \tau \quad (B-2)$$

The probability, $p(N)$, that the number of penetrations will be equal to or less than N is related to the average number of penetrations, $\bar{N}_>$, by the expression

$$p(N) = \sum_{k=0}^N \frac{\bar{N}_>^k e^{-\bar{N}_>}}{k!} \quad (B-3)$$

The parameters selected for use in the above equations are

$$\left. \begin{array}{l} \gamma = 2.0 \\ \phi = 1/2 \\ \theta = 2/3 \end{array} \right\} \text{ Meteoroid Penetration Parameters}$$

Contrails

$$\left. \begin{array}{l} \alpha = 3.5(10^{-10}) \text{ ft}^2\text{-hr} \\ \beta = 1.11 \end{array} \right\} \text{ Meteoroid Environmental Parameters}$$

$$E_t = 10.5(10^6) \text{ lb/in}^2 - \text{ Elastic Modulus of Target Material}$$

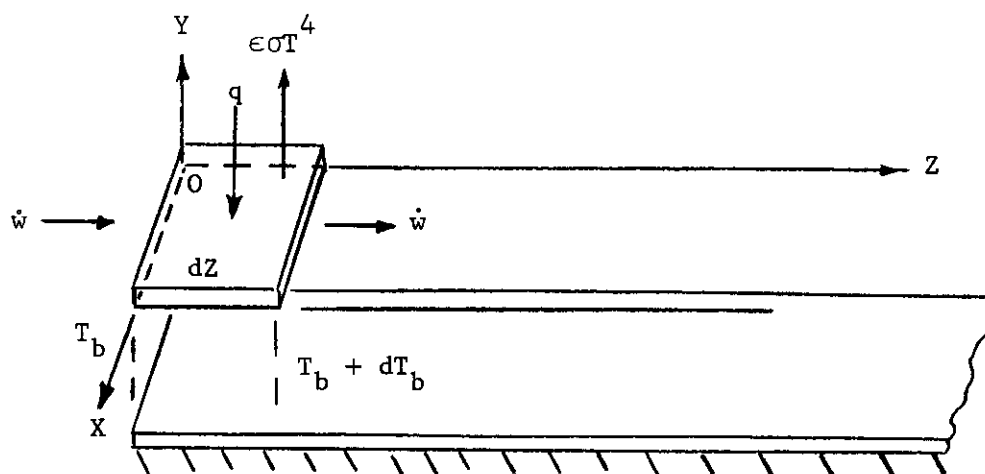
$$v = 40 \text{ km/sec} - \text{ Meteoroid Velocity}$$

When the skin gage thickness, t_s , and the mission parameter, $A\tau$, are related through the use of Equations (B-1), (B-2) and (B-3), the curves displayed in Figure 1 are obtained. Two skin gages, 0.040 and 0.050 were employed in the evaluation of the three sets of $p(N)$ curves. Curves have also been included in which $t_s = 0.100$ and 0.250 for $p(o)$. These latter curves demonstrate the requirements on skin thickness to achieve the high probabilities of no penetrations of relatively large surfaces exposed in space for modest periods of time.

APPENDIX C

TEMPERATURE REGULATION IN A DOUBLE-WALL SPACE VEHICLE BY CONVECTIVE HEAT TRANSFER

An analysis is presented indicating the required forced convective heat transfer to insure a specified temperature regulation in a duct exposed to thermal radiation in the ultrahigh vacuum of outer space. It is assumed in this analysis that the amount of heat transfer is controlled by the radiation mode of heat transfer and, hence, that conduction and convection resistance are negligible. This assumption is valid for many double-wall thermal applications. For a given initial gas temperature, the important parameters were found to be $(\epsilon \sigma x / \dot{w} c_p) Z$, α / ϵ , and the final gas temperature.



Assumptions:

- (1) Steady State
- (2) Negligible Temperature Gradient on the Inside Surface or Negligible Internal Energy Source or Sink

ENERGY BALANCE (q^+ out)

$$\begin{aligned} q_{\text{net}} &= -\dot{w} c_p dT_b \\ &= q_{\text{con}} = q_{\text{rad net}} \end{aligned} \quad (\text{C-1})$$

RATE EQUATION

$$q_{\text{rad}} = \epsilon \sigma T^4 \times dZ$$

$$q_{\text{irrad}} = - \left[\alpha q_s + \epsilon q_e \right] = -B \quad (\text{C-2a})$$

$$q_{\text{con}} = \frac{(T_b - T)}{R} \times dZ; \quad \text{where } R = \frac{1}{h_c} + \frac{y_o}{k}$$

$$q_{\text{rad net}} = - \left[\alpha q_s + \epsilon q_e \right] \times dZ + \epsilon \sigma T^4 \times dZ \quad (\text{C-2b})$$

therefore

$$\frac{T_b - T}{R} = -B + \epsilon \sigma T^4$$

Multiply by R and divide by $\epsilon \sigma T^4$ and rearrange terms,

$$\frac{T_b}{\epsilon \sigma T^4} = \frac{1}{\epsilon \sigma T^3} + R \left[\frac{-B}{\epsilon \sigma T^4} + 1 \right] \quad (\text{C-3})$$

A simple solution is obtained if,

$$\frac{1}{\epsilon \sigma T^3} \gg R \left[\frac{-B}{\epsilon \sigma T^4} + 1 \right] \quad (\text{C-4})$$

If this condition is true, the controlling heat transfer rate mechanism is radiation and

$$T \approx T_b \quad \text{and} \quad dT \approx dT_b$$

If

$$h_c \geq 1 \text{ BTU/hr-ft}^2\text{-}^\circ\text{F} \quad \text{and} \quad \frac{y_o}{k} \ll \frac{1}{h_c} \quad \left(\begin{array}{l} \text{True for most metals} \\ \text{where } y_o \leq 1 \text{ inch} \end{array} \right)$$

the above assumption is approximately true for $\alpha/\epsilon \leq 0.4$ and the assumption improves as α/ϵ is decreased. A large value of h_c reduces the constraint on α/ϵ .

Equating Equations (C-1) and (C-2b)

$$-\dot{w}c_p dT = \left[-(\alpha q_s + \epsilon q_e) + \epsilon \sigma T^4 \right] x dz$$

Divide both sides by $\epsilon \sigma$ and rearrange terms

$$\frac{dT}{(\frac{\alpha}{\epsilon} q_s + q_e) \frac{1}{\sigma} - T^4} = \frac{\epsilon \sigma x}{\dot{w}c_p} dz$$

$$\text{Let } D = \left(\frac{\alpha}{\epsilon} q_s + q_e \right) \frac{1}{\sigma} \quad (C-5)$$

Integrating between $T_{i(in)}$ and $T_{o(out)}$ and $Z = 0$ and $Z = Z$

$$\frac{\epsilon \sigma x}{\dot{w}c_p} Z = \frac{1}{4D^{3/4}} \left\{ \log \left| \frac{\left(\frac{D^{1/4}}{T_o} + 1 \right) \left(\frac{D^{1/4}}{T_i} - 1 \right)}{\left(\frac{D^{1/4}}{T_o} - 1 \right) \left(\frac{D^{1/4}}{T_i} + 1 \right)} \right| + 2 \left(\tan^{-1} \frac{T_o}{D^{1/4}} - \tan^{-1} \frac{T_i}{D^{1/4}} \right) \right\} \quad (C-6)$$

Therefore

$$\frac{\epsilon \sigma x}{\dot{w}c_p} Z = f(\alpha/\epsilon, T_o, T_i)$$

If the surface element is facing empty space, there is no irradiation and the differential equation simplifies to the following expression:

$$-\frac{dT}{T^4} = \frac{\epsilon \sigma x}{\dot{w}c_p} dz$$

Integrating from "i" to "o" gives

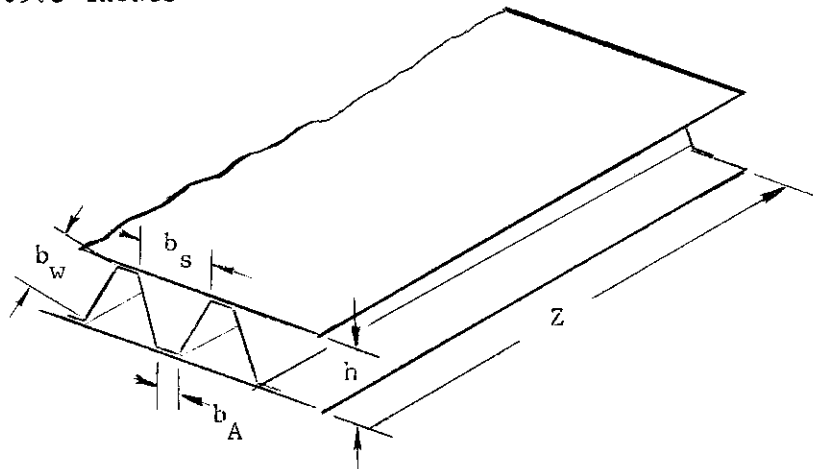
$$\frac{1}{T_o^3} - \frac{1}{T_i^3} = 3 \frac{\epsilon \sigma x}{\dot{w} c_p} Z \quad (C-7)$$

where

$$\frac{\epsilon \sigma x}{\dot{w} c_p} Z = f(T_o, T_i)$$

As is indicated in the derivation just presented, the assumption of a radiation rate-controlled process is implicit in Equation (C-6). Whenever results of Appendix C are used, Equation (C-4) should be evaluated to check the validity of this assumption. The following calculations are made to demonstrate the method of checking the assumptions of radiation rate-controlled process and the validity of the assumption for the representative structural design presented in Section 2.4.

$$\begin{aligned} h &= 1.41 \text{ inches} \\ b_A &= 0.59 \text{ inch} \\ b_s &= 1.48 \text{ inches} \\ b_w &= 1.41 \text{ inches} \\ Z = L &= 69.0 \text{ inches} \end{aligned}$$



Given:

$$\begin{aligned}\alpha/\epsilon &= 0.195 \\ \epsilon &= 0.77 \\ c_p &= 0.24 \text{ BTU/lb-}^\circ\text{R} \\ \dot{w} &= 0.036 \text{ lb/sec}\end{aligned}$$

REYNOLDS NUMBER CALCULATION

$$A = \frac{h}{2} (b_A + b_s) = 1.454 \text{ in}^2 (0.0101 \text{ ft}^2)$$

$$p_w = 2b_w + b_s + b_A = 4.89 \text{ in} (0.408 \text{ ft})$$

$$N_R = \frac{\rho V 4 r_h}{\mu} = \frac{4 \dot{w}}{\mu p_w} = 2.94 \times 10^4$$

where $\mu_{65^\circ\text{F}} = 1.2 \times 10^{-5} \text{ lb/ft-sec}$

CONVECTIVE FILM COEFFICIENT CALCULATION

Since the length of the duct considered here is quite long ($Z/4r_h > 50$), entrance effects on heat transfer can be neglected. For Reynolds numbers greater than 10^4 , the flow in the tube will be turbulent and the following expression can be used to calculate the convective film coefficient.

$$N_{st} N_{pr}^{0.5} = 0.022 N_R^{-0.2}$$

$$N_{pr} = \frac{c_p \mu}{k_{\text{Air}}} - 0.72$$

$$N_{st} = \frac{h_c}{\rho V \epsilon c_p} = \frac{h_c}{\frac{\dot{w}}{A} c_p}$$

where $\frac{\dot{w}}{A} = 3.57 \text{ lb/sec-ft}^2 \text{ (12,850 lb/hr-ft}^2\text{)}$

Therefore

$$h_c = 0.022 \frac{\dot{w}}{A} c_p \frac{N_R^{-0.2}}{N_{pr}^{0.5}} = 10.2 \text{ BTU/hr-ft}^2\text{-}^\circ\text{F}$$

RATE CONTROL ASSUMPTION

The criteria determining the applicability of Equation (C-6) is given in Equation (C-4) as

$$\frac{1}{\epsilon \sigma T^3} \gg R \left[\frac{-B}{\epsilon \sigma T^4} + 1 \right]$$

where

$$\frac{1}{\epsilon \sigma T^3} = 5.23 \text{ hr-ft}^2\text{-}^\circ\text{R/BTU}$$

and

$$R = \frac{1}{h_c} + \frac{y_o}{k} = 0.098 \text{ hr-ft}^2\text{-}^\circ\text{R/BTU}$$

where $k \text{ (aluminum)} = 120 \text{ BTU/hr-ft-}^\circ\text{R}$

If $\alpha/\epsilon = 0.4$, $q_s = 440 \text{ BTU/hr-ft}^2$ and $q_e = 60 \text{ BTU/hr-ft}^2$, then from Equation (C-2a)

$$B = 0.4(440) + 60 = 236 \text{ BTU/hr-ft}^2$$

Finally,

$$R \left[\frac{-B}{\epsilon \sigma T^4} + 1 \right] = 0.098 \left[\frac{-236}{100} + 1 \right] = 0.133 \text{ hr-ft}^2\text{-}^\circ\text{R/BTU}$$

For the case of no irradiation, $B = 0$ and

Contrails

$$R \left[\frac{-B}{\epsilon \sigma T^4} + 1 \right] = 0.098 \text{ hr-ft}^2\text{-}^\circ\text{R/BTU}$$

Since $5.23 \gg 0.133$ and 0.098 , the radiation rate controls the heat transfer process and Equation (C-6) is a realistic description of the process.